Elsevier Editorial System(tm) for Science of the Total Environment

Manuscript Draft

Manuscript Number: STOTEN-D-18-04778R2

Title: Research on the sustainable efficacy of g-MoS2 decorated biochar nanocomposites for removing tetracycline hydrochloride from antibiotic-polluted aqueous solution

Article Type: Research Paper

Keywords: Biochar-based nanocomposite; g-MoS2; Tetracycline hydrochloride; Sustainable application; Removal mechanisms

Corresponding Author: Professor Guangming Zeng, Ph.D.

Corresponding Author's Institution: Hunan University

First Author: Zhuotong Zeng

Order of Authors: Zhuotong Zeng; Shujing Ye; Haipeng Wu; Rong Xiao; Guangming Zeng, Ph.D.; Jie Liang; Chang Zhang; Jiangfang Yu; Yilong Fang; Biao Song

Abstract: Antibiotic concentrations in surface waters far exceed the pollution limit due to the abuse of pharmaceuticals, resulting in an urgent need for an approach with potential efficiency, sustainability and eco-friendliness to remove antibiotic pollutants. A novel biochar-based nanomaterial was synthesized by hydrothermal synthesis and was investigated for its removal potential for tetracycline hydrochloride (TC) from both artificial and real wastewater. The associative facilitation between biochar and g-MoS2 nanosheets was proposed, revealing the favorable surface structures and adsorption properties of the composite. The related adsorption kinetics, isotherms and thermodynamics were studied by several models with adsorption experimental data, turning out that biochar decorated by g-MoS2 exhibited optimum TC removal with adsorption capacity up to 249.45 mg/g at 298 K. The adsorption behavior of TC molecules on g-MoS2-BC can be interpreted well by three-step process, and it is dominated by several mechanisms containing pore-filling, electrostatic force, hydrogen bond and π-π interaction. In addition, the cost-effective g-MoS2-BC nanocomposites demonstrated excellent adsorption and recycling performance in TC-contaminated river water, which might provide the underlying insights needed to guide the design of promising approach for contaminant removal on a large scale in practical application.

Response to Reviewers: Response to decision letter (Ms. Ref. No.: STOTEN-D-18-04778R1)
Title: Research on the sustainable efficacy of g-MoS2 decorated biochar nanocomposites for removing tetracycline hydrochloride from antibiotic-polluted aqueous solution

Journal: Science of the Total Environment
Dear Prof. Ching-Hua Huang,

Thank you very much for your email on Jul 17, 2018, with regard to our manuscript (Ms. Ref. No.: STOTEN-D-18-04778R1) together with the requirement from you. According to the requirement, we have revised the language of manuscript carefully to meet the requirement of publication. We also responded the modification of grammar point by point as listed below. The revisions were highlighted in red so that you could easily identify them in the revised manuscript. We expect that you will be satisfied with our responses and revisions for the original manuscript. Once again, thank you very much for your suggestions.
Best regards and wishes.
Yours sincerely,
Guangming Zeng
Response to Editor:
I have carefully reviewed your revised manuscript. I feel you have adequately addressed most of the technical comments by the reviewers. However, your manuscript still requires substantial grammatical revisions in its present form, and that it cannot be accepted without addressing this concern. For this, we strongly recommend you to get somebody native in English language to perform the grammatical editing of your paper.

Response: Many thanks for your careful suggestion. We have revised the whole manuscript carefully and tried our best to avoid any grammar errors or badly worded/constructed sentences. In addition, we have asked the native English speakers of University of Northern British Columbia, Prof Jason Li (li@unbc.ca), and Texas A&M University, Dr Clark Zhang (hua.zhang@tamucc.edu), to check the English. We believe that the language now has been improved. Some revisions for better understanding are listed as follows:
(1) Highlights: "Pore structure and surface properties of biochar were improved by decorating with g-MoS2" was replayed by "Pore structures and surface properties of biochar were improved by decorated with g-MoS2" on line 21 of the revised manuscript.
(2) The sentence "Antibiotic level in surface waters is far exceeding the limits due to the abuse of pharmaceuticals, resulting in an urgent need for a potentially efficient, sustainable, and eco-friendly approach to remove antibiotic pollution" was replaced by "Antibiotic concentrations in surface waters far exceed the pollution limit due to the abuse of pharmaceuticals, resulting in an urgent need for an approach with potential efficiency, sustainability and eco-friendliness to remove antibiotic pollutants." on line 12-14 of the revised manuscript.
(3) The words "the removal potential of tetracycline hydrochloride" were revised as "its removal potential for tetracycline hydrochloride" on line 16 of the revised manuscript.
(4) The word "favourable surface structure" was revised as "favorable surface structures" on line 18 of the revised manuscript.
(5) The words "g-MoS2 decorated biochar" were replayed by "biochar decorated by g-MoS2" on line 21 of the revised manuscript.
(6) The words "actual aqueous contaminant removal on a large scale" were modified to "contaminant removal on a large scale in practical application" on line 28 of the revised manuscript.
(7) The word "threat" was revised as "threats" on line 37 of the revised manuscript.
(8) The words "high energy consumption, cost and toxic by-products as for chemical processes" were replayed by "high energy/cost consumption and toxic by-products as for chemical processes" on line 46-47 of the revised manuscript.
(9) The word "high" between "the" and "temperatures" on line 66 of the revised manuscript was deleted.

(10) The sentence "In order to get better efficiency, biochar is modified by metallic embedding, nanomaterial decorating and surface functionalization to remove antibiotics from aquatic solution by various mechanisms" was revised as "In order to get better removal efficiency for pollutants, biochar is modified by metallic embedding, nanomaterial decorating and surface functionalization based on various mechanisms" on line 66-68 of the revised manuscript.
(11) The words "huge deal of scientific interest" were revised as "huge deal of scientific interests" on line 86 of the revised manuscript.
(12) The words "…in removal antibiotics from aquatic environment" were modified to "…in antibiotic removal from aquatic environment" on line 91 of the revised manuscript.
(13) The words "to g-MoS2-BC" were revised as "on surface of g-MoS2-BC" on line 98 of the revised manuscript.
(14) The words "measuring a pH meter" were replayed by "measured by pH meter" on line 146-147 of the revised manuscript.
(15) The word "surface morphology and micro-structure" was changed to "surface morphologies and micro-structures" on line 175 of the revised manuscript.
(16) The word "for support of hierarchical MoS2 nanosheets" was revised as "for supporting hierarchical MoS2 nanosheets" on line 183 of the revised manuscript.
(17) The word "interaction" was modified to "interactions" on line 183 of the revised manuscript.
(18) The word "adsorption" was added before the "capacity" on line 210 of the revised manuscript.
(19) The words "…at this condition" were replaced by "…at pH in this range…" on line 307 of the revised manuscript.
(20) The words "as will be described below" were added after the "hydrophobic interaction (Chao et al., 2017)" on line 309 of the revised manuscript.
(21) The sentence "equalizing effect, which on one hand..." was revised as "equalizing effect: on one hand..." on line 320 of the revised manuscript.
(22) The words "were fit" were changed to "were fitted" on line 342 of the revised manuscript.
(23) The sentence "…pseudo-second-order model is more in agreement with the adsorption behavior across the whole experimental with significantly higher values of correlation coefficient" was modified to "…pseudo-second-order model is more consistent with the adsorption behavior across the whole experimental on the basis of the significant higher values of correlation coefficient " on line 350-352 of the revised manuscript.
(24) The words "possible rate controlling procedure affecting the kinetics of adsorption" were revised as "possible rate controlling adsorption process" on line 359-360 of the revised manuscript.
(25) The words "are consists of" were replayed by "are consisted of" on line 365 of the revised manuscript.
(26) The words "with initial TC concentration increasing" were modified to "with increasing initial TC concentration" on line 405-406 of the revised manuscript.
(27) The words "the facile and favorable adsorption is at all tested temperature" were revised as "the adsorption is facile and favorable at all tested temperature" on line 436-437 of the revised manuscript.
(28) The word "observing" was revised as "observed" on line 444 of the revised manuscript.
(29) The word "improved" was replaced by "improves" on line 457 of the revised manuscript.

(30) The word "influence" was revised as "the influences" on line 481 of the revised manuscript.
(31) The word "structure" was added after the "TC molecular" on line 497 of the revised manuscript.

**Type of contribution**: Original article

**Title**: Research on the sustainable efficacy of *g*-$MoS_2$ decorated biochar nanocomposites for removing tetracycline hydrochloride from antibiotic-polluted aqueous solution

Zhuotong Zeng [a, 1], Shujing Ye [b, 1], Haipeng Wu [a, b, c, 1], Rong Xiao [a,*], Guangming Zeng [a, b,*], Jie Liang [b], Chang Zhang [b], Jiangfang Yu [b], Yilong Fang [b], Biao Song [b]

[a] Department of Dermatology, Second Xiangya Hospital, Central South University, Changsha 410011, P R China

[b] College of Environmental Science and Engineering, Hunan University and Key Laboratory of Environmental Biology and Pollution Control (Hunan University), Ministry of Education, Changsha 410082, P.R. China

[c] Changjiang River Scientific Research Institute, Wuhan 430010, PR China

Contact information for authors:

Zhuotong Zeng

Mailing address: Second Xiangya Hospital, Central South University, Changsha, China. Email: zengzhuotong@csu.edu.cn. Phone: +86–731–88822754. Fax: +86–731–88823701.

Shujing Ye:

Mailing address: Environment Building, Hunan University, Lushan Road,

[*] Corresponding authors: Tel.: +86–731–88822754; fax: +86–731–88823701. Email address: zgming@hnu.edu.cn (Guangming Zeng) and xiaorong65@csu.edu.cn (Rong Xiao).

[1] These authors contribute equally to this article.

Changsha, China. Email: yeshujing0806@163.com. Phone: +86–731–88822754. Fax: +86–731–88823701.

Haipeng Wu:

Mailing address: Environment Building, Hunan University, Lushan Road, Changsha, China. Email: wuhaipeng0701@126.com. Phone: +86–731–88822754. Fax: +86–731–88823701.

Rong Xiao:

Mailing address: Second Xiangya Hospital, Central South University, Changsha, China. Email: xiaorong65@csu.edu.cn. Phone: +86–731–88822754. Fax: +86–731–88823701.

Guangming Zeng:

Mailing address: Environment Building, Hunan University, Lushan Road, Changsha, China. Email: zgming@hnu.edu.cn. Phone: +86–731–88822754. Fax: +86–731–88823701.

Jie Liang:

Mailing address: Environment Building, Hunan University, Lushan Road, Changsha, China. Email: liangjie@hnu.edu.cn. Phone: +86–731–88822754. Fax: +86–731–88823701.

Chang Zhang:

Mailing address: Environment Building, Hunan University, Lushan Road, Changsha, China. Email: zhangchang@hnu.edu.cn. Phone: +86–731–88822754. Fax: +86–731–88823701.

Jiangfang Yu:

Mailing address: Environment Building, Hunan University, Lushan Road, Changsha, China. Email: yooojf@163.com. Phone: +86–731–88822754. Fax: +86–731–88823701.

Yilong Fang:

Mailing address: Environment Building, Hunan University, Lushan Road, Changsha, China. Email: 15211096740@163.com. Phone: +86–731–88822754. Fax: +86–731–88823701.

Biao Song:

Mailing address: Environment Building, Hunan University, Lushan Road, Changsha, China. Email: songbiao@hnu.edu.cn. Phone: +86–731–88822754. Fax: +86–731–88823701.

# Response to decision letter (Ms. Ref. No.: STOTEN-D-18-04778R1)

**Title:** Research on the sustainable efficacy of *g*-$MoS_2$ decorated biochar nanocomposites for removing tetracycline hydrochloride from antibiotic-polluted aqueous solution

**Journal:** Science of the Total Environment

Dear Prof. Ching-Hua Huang,

Thank you very much for your email on **Jul 17, 2018**, with regard to our manuscript (Ms. Ref. No.: **STOTEN-D-18-04778R1**) together with the requirement from you. According to the requirement, we have revised the language of manuscript carefully to meet the requirement of publication. We also responded the modification of grammar point by point as listed below. The revisions were highlighted in red so that you could easily identify them in the revised manuscript. We expect that you will be satisfied with our responses and revisions for the original manuscript.

Once again, thank you very much for your suggestions.

Best regards and wishes.

Yours sincerely,

Guangming Zeng

**Response to Editor:**

I have carefully reviewed your revised manuscript. I feel you have adequately addressed most of the technical comments by the reviewers. However, your manuscript still requires substantial grammatical revisions in its present form, and that it cannot be accepted without addressing this concern. For this, we strongly recommend you to get somebody native in English language to perform the grammatical editing of your paper.

Response: Many thanks for your careful suggestion. We have revised the whole manuscript carefully and tried our best to avoid any grammar errors or badly worded/constructed sentences. In addition, we have asked the native English speakers of University of Northern British Columbia, Prof Jason Li (li@unbc.ca), and Texas A&M University, Dr Clark Zhang (hua.zhang@tamucc.edu) to check the English. We believe that the language now has been improved. Some revisions for better understanding are listed as follows:

(1) Highlights: "Pore structure and surface properties of biochar were improved by decorating with *g*-$MoS_2$" was replayed by "Pore structures and surface properties of biochar were improved by decorated with *g*-$MoS_2$" on line 21 of the revised manuscript.

(2) The sentence "Antibiotic level in surface waters is far exceeding the limits due to the abuse of pharmaceuticals, resulting in an urgent need for a potentially efficient, sustainable, and eco-friendly approach to remove antibiotic pollution" was replaced by "Antibiotic concentrations in surface waters far exceed the pollution limit due to the abuse of pharmaceuticals, resulting in an

urgent need for an approach with potential efficiency, sustainability and eco-friendliness to remove antibiotic pollutants." on line 12-14 of the revised manuscript.

(3) The words "the removal potential of tetracycline hydrochloride" were revised as "its removal potential for tetracycline hydrochloride" on line 16 of the revised manuscript.

(4) The word "favourable surface structure" was revised as "favorable surface structures" on line 18 of the revised manuscript.

(5) The words "*g*-$MoS_2$ decorated biochar" were replayed by "biochar decorated by *g*-$MoS_2$" on line 21 of the revised manuscript.

(6) The words "actual aqueous contaminant removal on a large scale" were modified to "contaminant removal on a large scale in practical application" on line 28 of the revised manuscript.

(7) The word "threat" was revised as "threats" on line 37 of the revised manuscript.

(8) The words "high energy consumption, cost and toxic by-products as for chemical processes" were replayed by "high energy/cost consumption and toxic by-products as for chemical processes" on line 46-47 of the revised manuscript.

(9) The word "high" between "the" and "temperatures" on line 66 of the revised manuscript was deleted.

(10) The sentence "In order to get better efficiency, biochar is modified by metallic embedding, nanomaterial decorating and surface functionalization to

remove antibiotics from aquatic solution by various mechanisms" was revised as "In order to get better removal efficiency for pollutants, biochar is modified by metallic embedding, nanomaterial decorating and surface functionalization based on various mechanisms" on line 66-68 of the revised manuscript.

(11) The words "huge deal of scientific interest" were revised as "huge deal of scientific interests" on line 86 of the revised manuscript.

(12) The words "…in removal antibiotics from aquatic environment" were modified to "…in antibiotic removal from aquatic environment" on line 91 of the revised manuscript.

(13) The words "to g-$MoS_2$-BC" were revised as "on surface of *g*-$MoS_2$-BC" on line 98 of the revised manuscript.

(14) The words "measuring a pH meter" were replayed by "measured by pH meter" on line 146-147 of the revised manuscript.

(15) The word "surface morphology and micro-structure" was changed to "surface morphologies and micro-structures" on line 175 of the revised manuscript.

(16) The word "for support of hierarchical MoS2 nanosheets" was revised as "for supporting hierarchical MoS2 nanosheets" on line 183 of the revised manuscript.

(17) The word "interaction" was modified to "interactions" on line 183 of the revised manuscript.

(18) The word "adsorption" was added before the "capacity" on line 210 of the revised manuscript.

(19) The words "…at this condition" were replayed by "…at pH in this range…" on line 307 of the revised manuscript.

(20) The words "as will be described below" were added after the "hydrophobic interaction (Chao et al., 2017)" on line 309 of the revised manuscript.

(21) The sentence "equalizing effect, which on one hand...” was revised as "equalizing effect: on one hand…" on line 320 of the revised manuscript.

(22) The words "were fit" were changed to "were fitted" on line 342 of the revised manuscript.

(23) The sentence "…pseudo-second-order model is more in agreement with the adsorption behavior across the whole experimental with significantly higher values of correlation coefficient" was modified to "…pseudo-second-order model is more consistent with the adsorption behavior across the whole experimental on the basis of the significant higher values of correlation coefficient " on line 350-352 of the revised manuscript.

(24) The words "possible rate controlling procedure affecting the kinetics of adsorption" were revised as "possible rate controlling adsorption process" on line 359-360 of the revised manuscript.

(25) The words "are consists of" were replayed by "are consisted of" on line 365 of the revised manuscript.

(26) The words "with initial TC concentration increasing" were modified to "with increasing initial TC concentration" on line 405-406 of the revised manuscript.

(27) The words "the facile and favorable adsorption is at all tested temperature" were revised as "the adsorption is facile and favorable at all tested temperature" on line 436-437 of the revised manuscript.

(28) The word "observing" was revised as "observed" on line 444 of the revised manuscript.

(29) The word "improved" was replaced by "improves" on line 457 of the revised manuscript.

(30) The word "influence" was revised as "the influences" on line 481 of the revised manuscript.

(31) The word "structure" was added after the "TC molecular" on line 497 of the revised manuscript.

# Research on the sustainable efficacy of *g*-$MoS_2$ decorated biochar nanocomposites for removing tetracycline hydrochloride from antibiotic-polluted aqueous solution

Zhuotong Zeng [a, 1], Shujing Ye [b, 1], Haipeng Wu [a, b, c, 1], Rong Xiao [a,*], Guangming Zeng [a, b,*], Jie Liang [b], Chang Zhang [b], Jiangfang Yu [b], Yilong Fang [b], Biao Song [b]

[a] Department of Dermatology, Second Xiangya Hospital, Central South University, Changsha 410011, P R China

[b] College of Environmental Science and Engineering, Hunan University and Key Laboratory of Environmental Biology and Pollution Control (Hunan University), Ministry of Education, Changsha 410082, P.R. China

[c] Changjiang River Scientific Research Institute, Wuhan 430010, PR China



[*] Corresponding authors: Tel.: +86–731–88822754; fax: +86–731–88823701. Email address: xiaorong65@csu.edu.cn (Rong Xiao) and zgming@hnu.edu.cn (Guangming Zeng).

[1] These authors contribute equally to this article.

**ABSTRACT**

Antibiotic concentrations in surface waters far exceed the pollution limit due to the abuse of pharmaceuticals, resulting in an urgent need for an approach with potential efficiency, sustainability and eco-friendliness to remove antibiotic pollutants. A novel biochar-based nanomaterial was synthesized by hydrothermal synthesis and was investigated for its removal potential for tetracycline hydrochloride (TC) from both artificial and real wastewater. The associative facilitation between biochar and *g*-$MoS_2$ nanosheets was proposed, revealing the favorable surface structures and adsorption properties of the composite. The related adsorption kinetics, isotherms and thermodynamics were studied by several models with adsorption experimental data, turning out that biochar decorated by *g*-$MoS_2$ exhibited optimum TC removal with adsorption capacity up to 249.45 mg/g at 298 K. The adsorption behavior of TC molecules on *g*-$MoS_2$-BC can be interpreted well by three-step process, and it is dominated by several mechanisms containing pore-filling, electrostatic force, hydrogen bond and π-π interaction. In addition, the cost-effective *g*-$MoS_2$-BC nanocomposites demonstrated excellent adsorption and recycling performance in TC-contaminated river water, which might provide the underlying insights needed to guide the design of promising approach for contaminant removal on a large scale in practical application.

**Keywords**: Biochar-based nanocomposite; *g*-$MoS_2$; Tetracycline hydrochloride; Sustainable application; Removal mechanisms

## 1. Introduction

Antibiotics, as emerging pollutants, are released into the environment in large quantities due to abuse of pharmaceuticals, and they have been detected excessively in surface water, ground water and sediment (Chao et al., 2014; Zhou et al., 2018). The existence of antibiotic residues in the environment has caused high concern because of their potential long-term adverse threats on human health and natural ecosystem (Ren et al., 2018; Ye et al., 2017b). There is an increasing demand for the removal of antibiotics from contaminated water to avoid the ecological risk. A growing number of researches have been explored for the remediation of antibiotics-contaminated water (Tiwari et al., 2017), containing biotechnology (degrading microorganism) (Chen et al., 2015; Ye et al., 2017a), chemical technology (oxidation, photo-catalysis) (Cheng et al., 2016; Wang et al., 2017) and physical technology (separation) (Gong et al., 2009; Wan et al., 2018; Xu et al., 2012b). However, some deficiencies restrict the application of these technologies, for instance, the growth-restricted microorganisms as for biological processes; high energy/cost consumption and toxic by-products as for chemical processes; and low efficiency as for pure physical separation (Ahmed et al., 2017; Tang et al., 2014). Tetracycline hydrochloride (TC) with amphoteric behavior, a kind of widely used antimicrobial, has been detected frequently in aquatic ecosystems, and it is difficult to degrade even with more toxic byproducts (Homem & Santos, 2011). Adsorption is a way that affects the migration-transformation of antibiotics in the aquatic environment, which is considered as a feasible and economical approach for

antibiotic removal (Chao et al., 2017; Liu et al., 2017).

Adsorbents play an important role in polluted water remediation, some common adsorbents and their modifications have been studied for removal of antibiotics from aqueous solution, such as graphene (Deng et al., 2013; Yang et al., 2017b), clay minerals (Long et al., 2011; Xu et al., 2012a), metal organic framework (Wang et al., 2018; Yang et al., 2018a, b), carbon nanotubes (Ji et al., 2009; Zhang et al., 2015) and powder activated carbon (Liu et al. 2017). Among them, biochar shows excellent adsorption performance as well as carbon sequestration based on its favorable physico-chemical surface characteristics, like high hydrophobicity and aromaticity, large surface area and developed pore structure (Liu et al., 2017; Ye et al., 2017a). Moreover, biochar is more environmentally and economically viable, since it is derived from the pyrolysis of waste biomass, allowing the resources recovery and utilization (Liang et al., 2017; Wu et al., 2017; Zeng et al., 2015). However, the effectiveness of biochar relies heavily on the temperatures and raw materials of production. In order to get better removal efficiency for pollutants, biochar is modified by metallic embedding, nanomaterial decorating and surface functionalization based on various mechanisms (Tan et al., 2015; Ye et al., 2017b). Zhang et al. (2012) prepared an engineered graphene-coated biochar, and the results showed the adsorbed amount of contaminant on the graphene-coated biochar was enhanced by the strong π-π interaction between aromatic structure of pollutant molecules and graphene sheets on biochar surface, which was more than 20 times higher than that of the pristine biochar (Zhang et al.,

2012). It is still a challenge to develop a cost-effective adsorbent for water treatment on large scale application, along with the difficulties in separation and regeneration of used adsorbent.

Molybdenum disulfide with a special layered structure (*g*-$MoS_2$) is a novel quasi-two-dimensional lamellar nanomaterial similar to graphene, which had been proposed as a potential alternative for removal of antibiotics (Chao et al., 2017; Chao et al., 2014; Han et al., 2017; Theerthagiri et al., 2017). A $MoS_2$ molecule possesses the S-Mo-S sandwich structure with the Mo atom sandwiched between two S atoms. Due to the large surface area, surface covalent forces and strong edge effects (Kiran et al., 2014), the researches of *g*-$MoS_2$ in contaminant adsorption (Chao et al., 2014; Qiao et al., 2016), electrochemical performance (Voiry et al., 2013; Wang et al., 2016), and catalytic degradation (Vattikuti & Byon, 2016; Zhu et al., 2016), etc. have drawn huge deal of scientific interests. However, *g*-$MoS_2$ nanosheets have relatively low dispersibility and tend to agglomerate, thereby adversely affecting the remediation efficiency as well as having bad impacts on aquatic organisms. Until now, no systematic study concerning the adsorption performance of $MoS_2$ nanomaterial-decorated biochar (biochar is used as substrate and is modified to a nanocomposite with *g*-$MoS_2$ nanosheets) in antibiotic removal from aquatic environment has been published yet.

In this work, a novel adsorbent of *g*-$MoS_2$ nanosheet-decorated biochar (*g*-$MoS_2$-BC) was synthesized firstly using a facile hydrothermal method. Batch

adsorption experiments were designed to investigate the adsorption performance of the composite in aqueous solution that contaminated with tetracycline hydrochloride (TC). The main aims of the research were to 1) synthesize and characterize the *g*-$MoS_2$-BC; 2) explore the adsorption behavior of TC on surface of *g*-$MoS_2$-BC, including the adsorption kinetics, isotherms, thermodynamics, mechanisms as well as the factors potentially affecting the adsorbed amount; and 3) investigate the removal efficiency of *g*-$MoS_2$-BC applied in real TC wastewater.

## 2. Materials and methods

### 2.1. Materials

Rice straw was obtained from bottomland of Dongting Lake, located in Changsha, China. Tetracycline hydrochloride (TC, purity >98.5%), sodium molybdate and thioacetamide were purchased from Shanghai Chemical Corp and used without purification. Besides, deionized water (18.25 MΩ/cm) used in the experiment was produced by an Ulupure (UPRII-10 T) laboratory water system.

### 2.2 Preparation of *g*-$MoS_2$-decorated biochar

As shown in Fig. 1, biochar was produced by slow pyrolysis of agricultural straw in tube furnace operating at a continuous flow of $N_2$ gas and a temperature of 500 °C for a residence time of 2 h, according to previous research (Zeng et al., 2015). In a typical synthesis of the $MoS_2$ nanosheets, 230 mg of $Na_2MoO_4 \cdot 2H_2O$ and 460 mg of thioacetamide were dissolved in 60 mL deionized water, in which 0.1 g of the prepared biochar and 0.1 mM PEG10000 were added in sequence with magnetic stirring, and the

mixture dispersed via ultrasonication for 30 min. Afterwards, the whole solution was transferred to a 100 mL Teflon-lined autoclave and heated up to 180 °C for 24 h by hydrothermal treatment. After the mixture was cooled to room temperature naturally, the black solid precipitate (*g*-$MoS_2$-BC) produced in the solution was collected by centrifugation (8000 rpm for 5 min), and then was washed six times with anhydrous ethanol and deionized water, thereby drying in an oven at 80 °C for overnight.

2.3. Characterization methods

The field emission scanning electron microscope (SEM, JSM-6700F, Japan) equipped with an energy dispersive X-ray analyzer (EDS, AMETER, USA) was used to examine the surface morphology and elemental compositions of the *g*-$MoS_2$-BC. The structural details of the composite were further characterized by the transmission electron microscopy (TEM). The BET specific surface area and pore characteristics were calculated based on the $N_2$ adsorption-desorption isotherms at 77.3 K by using automatic surface and porosity analyzer (Quantachrome, USA). Fourier transform infrared spectrum (FT-IR) measurements, recorded in the range of 4000-400 $cm^{-1}$, were performed in KBr pellet by Nicolet 5700 Spectrometer, USA. The X-ray diffraction (XRD) patterns were showed by Bruker AXS D8 Advance diffractometer equipping with a Cu-K*a* radiation source (λ=1.5417 Å) to explore the crystal structures of as-synthesized composite. Binding energies of the material elements were conducted based on the X-ray photoelectron spectroscopy (XPS, Thermo Fisher Scientific-K-Alpha 1063, UK), with the calibration of C1s at 284.8 eV.

Thermogravimetric analysis (TGA) was carried out under nitrogen flow with a heating rate of 10 °C/min (TG209, Netzsch, Shanghai, China). The zeta potentials analysis of *g*-$MoS_2$-BC and TC were determined using Electroacoustic Spectrometer (ZEN3600 Zetasizer, UK) at solution pH ranging from 2.0 to 11.0.

2.4. Adsorption and removal of TC by *g*-$MoS_2$-BC

The batch experiments were carried out in 100 mL Erlenmeyer flasks containing the mixture of 20 mg *g*-$MoS_2$-BC and 50 mL TC aqueous solution. All flasks were wrapped with aluminum foils to avoid photodegradation and then placed in a thermostatic water shaking bath at an agitation speed of 150 rpm. The desired pH of solution were achieved by the adjustment with 0.1 M NaOH or 0.1 M HCl measured by pH meter (PHSJ-5, China), varying from 2.0 to 11.0 in initial TC solution (100 mg/L). The effect of salt ionic strength on the removal of TC (100 mg/L) was studied with the sodium chloride (NaCl) and calcium chloride ($CaCl_2$) at concentration range of 0-0.1 M. After shaking under 298 K for 24 h, the samples were taken from the flasks, followed by centrifuged and filtered using 0.45 μm PVDF disposable filters prior to UV spectrophotometry (UV-2550, SHIMADZU, Japan) at $\lambda_{max}$ 357 nm.

Adsorption kinetics studies were carried out by mixing 20 mg of as-synthesized composite and 50 mL TC solution with initial concentration of 50, 100, 150 mg/L at pH of 4.0. The solution was shaken with a speed of 150 rpm at temperature of 298 K, and samples were taken at predetermined time intervals (from 5 min to 30 h) for the determination of TC residual concentration after filtration. Adsorption isotherm and

thermodynamic experiments of *g*-$MoS_2$-BC were performed under three different temperatures (298, 308, and 318 K). 50 mL TC solutions with different initial concentrations ranging from 10 to 400 mg/L were adjusted to pH at 4.0 and then mixed with 20 mg composite for shaking. The TC concentrations of sample were then determined by above-mentioned ultraviolet spectrophotometry method after centrifugation and filtration.

The research on practical application of *g*-$MoS_2$-BC in real water samples (river water: obtained from Xiang River located in Changsha for TC solution preparation without filtration) was conducted by mixing 20 mg of *g*-$MoS_2$-BC with 50 mL real wastewater polluted by TC (100 mg/L), and the mixture was shaken at 298 K for 24 h. The regeneration of *g*-$MoS_2$-BC was carried out by adding TC-loaded *g*-$MoS_2$-BC to 50 mL NaOH (0.2 mol/L) and stirring the mixture at temperature of 298 K and agitation speed of 140 r/min for 24 h. The suspension liquid was centrifuged after desorption, and the collected solid (regenerated *g*-$MoS_2$-BC) was dried at 353 K and applied for next round of adsorption experiment with four-times repetition.



## 3. Results and discussion

### 3.1 Characterization of *g*-$MoS_2$-BC composite

The surface morphologies and micro-structures of the manufactured materials were examined by SEM and TEM. The SEM image of pristine biochar (Fig. 2a) shows essentially the smooth surface morphology composing of closely packed tubular structures with a cavity size of 1-2 μm. Upon the modification, the resulting

*g*-$MoS_2$-BC composite was found to be relatively uneven surface decorated with $MoS_2$ stacking hierarchical structure. A high magnification SEM image of the composite, presented in Fig. 2c, reveals that the tubular carbon material is disorderly assembled by crumpled nanosheets with curved edges, indicating the biochar could be regarded as a fresh substrate for supporting hierarchical $MoS_2$ nanosheets. The interactions between the oxygen-containing functional groups of biochar and $Mo^{4+}$ precursors might be responsible for the *in situ* growth of $MoS_2$ nanosheets on biochar surface (Chang & Chen, 2011; Zhao et al., 2017). Compared with the bulk structure of pure $MoS_2$ (Fig. 2b), the $MoS_2$ in composite (Fig. 2d) exhibits cluster framework with relatively few layers stacking, which is conducive to the exposure of active sites with defect-rich structure. The TEM images (Fig. S2) and HRTEM (Fig. e and f) further confirm a hierarchical crumpled and disordered structure with curved edges onto the carbon-based materials. HRTEM image illustrates the discontinued fringes of the curled edges, indicating the defect-rich structure with ample surface sites (Qiao et al., 2017). The lattice fringes of *g*-$MoS_2$ on composite display interplanar spacing of ~ 0.67 nm, the different interlayer distances should be associated with the intercalation of $MoS_2$ nanosheets and biochar.

In order to examine the porous properties of *g*-$MoS_2$-BC composite, Brunauer-Emmett-Teller (BET) gas sorptometry measurement was conducted. The inset of Fig. 3a describes the $N_2$ adsorption/desorption isotherm of the composite, which can be identified as type IV isotherm with a hysteresis loop, demonstrating the

mesoporous characteristic of *g*-$MoS_2$-BC. The observed large hysteresis loop is intermediate between typical H3- and H4-type isotherm, which is considered to be derived from the stack of laminated layered structure of the slit pore. The corresponding pore-size distribution, obtained from the isotherm by using the BJH method and shown in Fig. 3a, elucidates that most of the pores fall into the size range of 2 to 20 nm and the average pore diameter is calculated to be 3.509 nm. It is well established that adsorbent might exhibit the best adsorption performance when its pore diameter is 1.7-3 times larger than the adsorbate molecular size (even more than 3-6 times if adsorbent needs to be recycled) (Tang et al., 2018). Taking the TC molecule dimension (1.41 nm long, 0.46 nm wide and 0.82 nm high) into account, we conclude that *g*-$MoS_2$-BC composite is endowed with adsorption capacity for efficient TC molecular removal based on their pore-size distribution. On the whole, the prepared composite exhibits a BET specific surface area of 176.8 $m^2/g$ and a pore volume of 0.0839 $cm^3/g$. Both are higher than the corresponding value of the pristine biochar, it should be noted that the change could be attributed to the extra mosaic structure of $MoS_2$ nanosheets with plenty of folded edges like wings.

The X-ray powder diffraction (XRD) patterns of the as-prepared $MoS_2$ and *g*-$MoS_2$-BC composite are shown in Fig. 3b. The three detected diffraction peaks are indexed to (002), (100) and (110) planes, respectively, indicating a hexagonal phase of $MoS_2$ (JCPDS card No. 37–1492) (Chao et al., 2014). Subtle changes in the peak location may be due to the strain effect by bending of the layers or lattice expansion

introduced by crystal defects (Berdinsky et al., 2005). Especially, the (002) diffraction peak, resulted primarily from the scattering of interlayer Mo–Mo (Yang et al., 2017a), is feeble in the pattern, suggesting that $MoS_2$ is consisted of only a few layers nanosheets. There is no obvious difference in peak position between pure $MoS_2$ and the *g*-$MoS_2$-BC composite due to the low XRD intensity of biochar, which also reveals that the chemical composition of $MoS_2$ has not changed after the surface modification. From the variation in width and strength of (002) plane diffraction peak, it can be observed that the growth of $MoS_2$ crystal along the *c*-axis in composite is inhibited owing to the presence of biochar, demonstrating fewer stack of $MoS_2$ layers.

FT-IR analysis was carried out to investigate the surface property of the BC and *g*-$MoS_2$-BC composite. It can be seen from the Fig. 3c, several characteristic FT-IR peaks of biochar are observed in composite, including 3384-3450 $cm^{-1}$ for O–H stretching, 2860 $cm^{-1}$ for C–O of carboxyl, 2365 $cm^{-1}$ for cumulated double bonds stretching, 1635 $cm^{-1}$ for C=C vibration, 1446 $cm^{-1}$ for aromatic benzene ring skeletal vibration, 1247 $cm^{-1}$ for C–O stretching, 1039 and 1095 $cm^{-1}$ for C–O–C pyranose ring skeletal vibration, 858 $cm^{-1}$ for C–H bending vibrations and 667 $cm^{-1}$ for S–H vibration. In addition to the common functional groups above mentioned, a new stretch at 617 $cm^{-1}$ appearing in curve (II) is assigned to $\gamma_{as}$ Mo–S vibration (Wang et al., 2016), demonstrating the successful bindidng of $MoS_2$ onto the biochar surface. Moreover, another fresh peak presenting at 916 $cm^{-1}$ in curve (II) could be ascribed to the stretching vibration of Mo=O (Han et al., 2017), which implies the partial oxidation

of the Mo atom on edge of nanosheet. Curve (III) in the Fig. 3c describes the FT-IR spectrum of TC-loaded *g*-$MoS_2$-BC, the enhanced and broadened peaks approximately at 3500 to 3900 $cm^{-1}$ are probably originated from the extra functional groups of TC molecule, especially the peak around 3520 $cm^{-1}$ corresponding to the acylamino of TC. These observations confirmed that the TC molecules are successfully adsorbed on the surface of *g*-$MoS_2$-BC composite.

X-ray photoelectron spectroscopy (XPS) was performed to further investigate the surface chemical composition and valence state of the elements in *g*-$MoS_2$-BC composite. The survey spectrum, presented in Fig. 3d, reveals the *g*-$MoS_2$-BC composite is composed of four major elements of C, O, Mo, and S. Compared with the biochar before and after modification, besides the introduction of Mo, and S elements in *g*-$MoS_2$-BC, the proportion of oxygen in the element composition is observed to increase, which implies that more oxygen-containing functional groups appear on composite surface. In the high resolution XPS spectrum of Mo 3d, shown in Fig. 4a, two peaks locating at 232.30 eV and 229.00 eV can be assigned to Mo $3d_{3/2}$ and Mo $3d_{5/2}$, respectively, characterizing of $Mo^{4+}$ in 1T-$MoS_2$, while the doublet peaks presenting at about 233.28 and 229.76 eV are attributed to the $3d_{3/2}$ and $3d_{5/2}$ of $Mo^{4+}$ in 2H–$MoS_2$ (Qiao et al., 2016). Meanwhile, two weak peaks centering at 236.17 and 232.90 eV are attributed to the oxidation state $Mo^{6+}$, which might be derived from the slight oxidation of Mo atoms at the defect or edges of $MoS_2$ nanosheets due to the high oxidation activity (Zhou et al., 2014). The peaks at 163.80 and 162.20 eV (Fig. 4b)

could be indexed to S 2p1/2 and S 2p3/2 orbital of divalent sulfide, respectively, suggesting the valence state of S element is -2. In combination with another analysis of peak at 226.66 eV (Fig. 4a) arising from S 2s, the existence of $MoS_2$ on the composite is confirmed. In the C 1s XPS spectrum (Fig. 4c) of composite, the C 1s band is deconvoluted into four peaks locating at 284.50, 284.83, 286.45, and 287.36 eV, assigning to the binding of C=C/C–C, CO/Mo, C–O and C=O, respectively. The binding energies of O 1s peaks (Fig. 4d) are observed at about 532.90, 531.30 and 533.51 eV, corresponding to the O–C/O–H, O–Mo and O=C, respectively, which are consistent with the FT-IR results.

The thermal stability of the prepared materials was examined by TGA which is shown in Fig. S3. The weight percentage of both materials was observed to decrease with increasing temperature from 20 to 800 °C. Compared with the pristine biochar, modified biochar has considerably high thermal stability before 450 °C with an approximate 5% weight loss. However, the weight percentage of *g*-$MoS_2$-BC dropped sharply after 500 °C, which could be attributed to the decomposition of the loaded $MoS_2$ and organic species that adsorbed on material surface during synthesis process.

**3.2 Effect of pH on TC adsorption**

It is generally believed that pH plays an important role in influencing adsorption capacity by changing both surface properties of adsorbent and adsorbate. The effect of solution pH varying from 2.0 to 11.0 on TC adsorption to *g*-$MoS_2$-BC was investigated, and the corresponding results with the zeta potential of *g*-$MoS_2$-BC are measured and

illustrated in Fig. 5a. It could be observed that the adsorption capacity exhibits increasing trend when pH value changes from 2.0 to 4.0, but the effect is little when pH value in the range of 5.0-7.0, sequentially, the declining trend of adsorption capacity is obvious especially when pH value >8.0.

The surface charge of *g*-$MoS_2$-BC, which makes great influences on the adsorption process of TC, is sensitive to the solution pH value. According to the result obtained by Fig. 5a, the zero potential point ($pH_{ZPC}$) of *g*-$MoS_2$-BC is around 3.21, the adsorbent surface shows electronegative and decreases gradually with increasing pH value when $pH>pH_{ZPC}$, owing to the dissociation of carboxylic group on the surface of *g*-$MoS_2$-BC. Besides the charge change of adsorbent surface, the chemical speciation of organic compound also transforms by the protonation/deprotonation transition of functional groups at different pH (Tan et al., 2016a). Tetracycline is amphoteric molecule along with multiple ionizable functional groups, which exists cations ($TCH_3^+$: derived from protonation of the dimethyl-ammonium group), zwitterions ($TCH_2^0$: derived from deprotonation of the phenolic diketone moiety), and anions ($TCH^-$ and $TC^{2-}$: derived from deprotonation of the tri-carbonyl groups and phenolic diketone moiety) in accordance with the different dissociation constant ($pK_a$=3.4, 7.6 and 9.7) (Chao et al., 2017). When the pH value is below 3.21, both surface Zeta potential of TC and *g*-$MoS_2$-BC composite are positive and decrease with the increasing pH value of the solution, demonstrating the weakening effect of the electrostatic repulsion which is favorable for adsorption. TC is predominantly existed as zwitterion at pH values

ranging of 4.0-7.0 with almost no net electrical charge, resulting in little electrostatic interactions (attraction or repulsion) and unobvious effect of pH changing on the adsorption capacity. The comparatively large adsorption capacity at pH in this range may be determined by other interactions, such as hydrogen bond, π-π and hydrophobic interaction (Chao et al., 2017), as will be described below. Nevertheless, when pH value is >8, the negatively charged surface of *g*-$MoS_2$-BC is generally decreases and presents an enhancing electrostatic repulsion to anions $TCH^-$ and $TC^{2-}$, which adversely affects the adsorbed amount of TC.

### 3.3 Effect of ionic strength on the adsorption capacity

In order to get closer to the actual situation of natural water, different amounts of sodium chloride and calcium chloride ranging from 0-0.1 mol/L were added to solution to explore the influences of ionic strength on the adsorption capacity. As can be seen from Fig. 5b, the addition of extra ions slightly decreases the adsorbed amount of TC in generally, while the adsorption capacity changes very little with the increasing NaCl concentration. There are two possible reasons accounted for the slight change: (1) equalizing effect: on one hand, the $Na^+$ ions inhibit the electrostatic interaction between the TC cations with *g*-$MoS_2$-BC groups by competition (Wu et al., 2014); on the other hand, the salt would be beneficial for the dissociation of TC molecules to $TC^+$ by facilitating the protonation and result in promoting electrostatic interaction (Tan et al., 2016b). And (2) electrostatic interaction is only a considerably weak mechanism that affects the adsorption of TC on *g*-$MoS_2$-BC. However, the downtrend is evident

and it represents obvious inhibiting effect of TC adsorption with the increase of $CaCl_2$ concentration. This difference may arise from much higher screening effect by $CaCl_2$ on the electrostatic interaction compared with NaCl, and thus more actives sites are occupied by $Ca^{2+}$, which confirms the electrostatic interaction has a certain degree in the domination of adsorption.

### 3.4 Effect of time and adsorption kinetics

As shown in Fig. 6a, the adsorption of TC by *g*-$MoS_2$-BC is a time-dependent process, which could be divided into two phases: fast- and slow- adsorption stages. Attributed to the abundant active sites and attractive electrostatic force on composite surface for TC molecules, it is found that the adsorbed amount increased as the increasing contact time, and nearly 85% of the adsorption capacity was accomplished within the first 4 h, which is defined as fast-adsorption stages. Then, the adsorption was performed at much lower rate. The adsorption rate went down gradually until there was no significant variation in the adsorbed amount after 24 h, which represents that the adsorption equilibrium has been achieved.

In order to further analyze the kinetics of TC adsorption onto *g*-$MoS_2$-BC, the experimental data were fitted by pseudo-first-order, pseudo-second-order, intra-particle diffusion, Boyd's film-diffusion and Bangham channel diffusion models at three different initial TC concentrations to research the characteristics of the adsorption process in this study. The linear forms of these kinetic models are presented in Table S1, and the related kinetic parameters calculated by linear regression are summarized in

Table 1 and Table 2.

The pseudo-first-order and pseudo-second-order models are two universal model widely used for investigation of the adsorption kinetics. Compared with the pseudo-first-order model, pseudo-second-order model is more consistent with the adsorption behavior across the whole experimental on the basis of the significant higher values of correlation coefficient (Table 1). This is also supported by the favorable fitting between the equilibrium adsorption capacity obtained from experimental data ($q_{e,exp}$) and the calculated values ($q_{e,cal}$) in pseudo-second-order model, suggesting the adsorption behavior is much affected by chemical mechanism. It should also be mentioned that the pseudo-second-order rate constants ($k_2$) reduces with increasing initial TC concentration, which could be attributed to the low competition of TC molecules for adsorption sites at lower initial concentration.

To achieve a better understanding of the diffusion mechanisms and possible rate controlling adsorption process, Intra-particle diffusion, Boyd's film-diffusion and Bangham channel diffusion model were further applied. Intra-particle diffusion model, an empirically functional relationship of adsorbed amount, is used to analyze experimental data with some crucial parameters (intra-particle diffusion rate constant $k_{id}$, and $C_i$ related to the thickness of boundary layer). As can be seen from part d of Fig. 6, the plots of $q_t$ against $t^{1/2}$ are consisted of three linear sections, indicating that the TC adsorption processes are associated with multiple steps. High linear correlation coefficient and all non-zero $C_i$ values, presented in Table 2, imply that intra-particle

diffusion is involved in the adsorption process, while it is not the only rate-controlling step (Wu et al., 2014). The first linear section with a relatively sharp slope demonstrates the transport of TC from bulk solution to the external surface of *g*-$MoS_2$-BC, which is controlled by the molecule diffusion and film diffusion. The second section with slow slope describes the gradual adsorption stage, where the intra-particle diffusion dominates, that is, the diffusion of the TC molecules transfer into the pores of *g*-$MoS_2$-BC from its external surface. The last linear section with tardy slope implies the arrival of adsorption equilibrium. Comparing the rate constant of three stages, $k_{1d}$ is much larger than other two values, indicating that the film diffusion of TC molecules transferring through the boundary liquid layer is the most important limiting step of the adsorption. The wing-like *g*-$MoS_2$ with a quasi-two-dimensional few-layered structure, embedded in the biochar surface, helps TC molecules reach the active sites of surface more easily, since the TC molecules only need to divert from liquid phase through the boundary liquid membrane, but barely need to transfer in limited intermediate layer (Chao et al., 2017).

To shed light on the actual rate-controlling step participated in the overall TC adsorption process, the Boyd's film-diffusion and Bangham channel diffusion model were used to illustrate the experimental data. On the basis of these models, the linearity of the plots provides the fairly reliable information to define the actual rate-controlling step as film diffusion or intra-particle diffusion. The plots of calculated $B_t$ versus time t for early stage of first 8 h are the segment-line which do not pass through the origin,

suggesting that the rate-controlling step is dominated by film diffusion at the initial stage of adsorption process, subsequently took over by other mechanisms (intra-particle diffusion). Furthermore, the relatively good linear coefficients of Bangham channel diffusion model, presented in Table 1, reveal the performance of channel diffusion behavior in this adsorption process. In general, the adsorption of TC onto the surface of *g*-$MoS_2$-BC includes three steps: (1) the TC molecules overcome the liquid resistance and transfer from the solution phase to the exterior surface of *g*-$MoS_2$-BC controlled by film diffusion; (2) the TC molecules migrate on the surface and enter the pores of particles, as the adsorbent particles are loaded with TC; and (3) the TC molecules that arrived at the active site are absorbed on the interior surface of *g*-$MoS_2$-BC and gradually reach the adsorption equilibrium.

**3.5 Adsorption isotherms**

The isotherm plays an important role in designing the adsorption system, which shows the distribution of solute molecules in solution phase and solid phase upon adsorption reaching equilibrium. The relationship between the equilibrium adsorption capacity ($q_e$) and equilibrium TC concentration ($C_e$) in solution, presented in Fig. S4a, shows the adsorption capacity of *g*-$MoS_2$-BC enhances with increasing initial TC concentration in the range of 10-400 mg/L. This may be explained by the more powerful driving force provided by higher initial TC concentration to overcome the mass transfer resistances between aqueous and solid phases (Qiao et al., 2016). To further explore the isotherms, the adsorption equilibrium data at temperature of 298,

308, and 318 K were fitted by different equilibrium models including Langmuir, Freundlich, Temkin, BET isotherm and Dubinin-Redushckevich (D-R) isotherm models. The forms of these isotherm models and their related isotherm parameters are presented in Table S1 and Table 3, respectively.

The Langmuir model, based on the assumption of monolayer adsorption on specific homogenous sites without interactions between molecules, is shown in the Fig. S4b. The linear relation is obtained from $C_e/q_e$ against $C_e$ with highest correlation coefficients, revealing that the adsorption of TC onto *g*-$MoS_2$-BC probably is monolayer molecular adsorption associated with the functions of chemical mechanism. Concerning the different temperature, the parameters $q_{max}$ and $k_L$ increases as temperature rises up, implying higher temperature is likely to inspire adsorption through enhancing the bond energy between TC molecules and surface sites (Tang et al., 2018). It is noteworthy that a critical characteristic, the dimensionless constant separation factor $R_L$, is found to be between 0 and 1, which suggests that the adsorption process is favorable. As an improvement of the Langmuir model, the BET adsorption isotherm model is based on the assumption that the adsorbates are randomly adsorbed on a homogeneous surface to form a multi-molecular layer without horizontal interaction. The TC adsorption equilibrium data is fitted better by BET model (inset of Fig. S4b) with higher correlation coefficient (Table 3), demonstrating the adsorption on *g*-$MoS_2$-BC surface may be multilayer formation (Jahangiri-Rad et al., 2013).

Freundlich model is an empirical formula which assumes that there are multilayers

of adsorbate on heterogeneous surface. It can fit the experimental data well as indicated by the good correlation coefficients ($R^2$ > 0.948), suggesting that the physical interaction also takes part in the TC adsorption on *g*-$MoS_2$-BC surface. The $K_F$ value, represented the adsorption capacity, was observed to increase with the increasing temperature. An essential parameter, heterogeneity factor *1/n*, is used to describe the bond distribution, and all *1/n* values are less than 1, suggesting the adsorption is facile and favorable at all tested temperature. On the whole, the adsorption behavior of TC molecular onto the *g*-$MoS_2$-BC surface is determined by the combined impacts of the physical and chemical mechanisms.

In contrast to the models mentioned above, the Temkin isotherm model assumes that the adsorption heat of the adsorbate on the surface decreases linearly with increasing coverage, which is closer to the actual state of the adsorption experiment. As shown in Fig. S4d, the linear regression plot of $q_e$ versus $lnC_e$ is relatively weak observed by the correlation coefficients ($R^2$) in range of 0.915-0.965, which reveals that the chemical mechanism is not the only controlled interaction for the TC adsorption behavior. This is consistent with the calculated values of $b_T$ (related to the heat of adsorption) in Table 3, since the low $b_T$ value reflects the comparatively weak chemical interaction between TC molecules and surface of *g*-$MoS_2$-BC (Wu et al., 2014). Finally, the D-R isotherm model was also analyzed in its linearized form regarding to the TC concentration at equilibrium. The calculated sorption free energy values (*E*) shown in Table 3 are lower than 8, confirming the occurrence of physical

adsorption behavior of TC molecular. However, given the relatively small correlation coefficient, the physical driving force is considered to have a limited role in TC adsorption process.

### 3.6 Thermodynamic analysis

As can be seen from part a of Fig. S4, temperature is observed to have a significant effect on TC adsorption behavior. The adsorption capacity improves obviously with the increasing temperature, and the average adsorption capacity increases from 174.701 mg/g at 298 K to 226.653 mg/g at 318 K with about 30% rises under initial TC concentration of 100 mg/L, which suggests that the adsorption is an endothermic process. High temperature is favorable for adsorption, due to the swelling effect on the particle porosity which makes the pore volume allow TC molecules to rapidly diffuse through the external boundary layer and within interior pore of *g*-$MoS_2$-BC. The adsorption of TC under different temperature was investigated to make clear the thermodynamic property. Related parameters containing the Gibbs free energy ($\Delta G^o$), enthalpy ($\Delta H^o$), and entropy ($\Delta S^o$) were determined by Gibbs-Helmholtz equation. All negative values of $\Delta G^o$, shown in Table S2, confirm that the absorption process of TC molecules on *g*-$MoS_2$-BC surface is spontaneous and feasible, and it is observed to decrease from -4.649 kJ/mol to -9.129 kJ/mol as the temperature increasing, manifesting that the adsorption is more favorable at higher temperature. The $\Delta G^o$ value is in the range of -20~0 kJ/mol, confirming again the role of physical interactions in this adsorption process. Based on the positive value of $\Delta H^o$, we prove

the endothermic nature of TC adsorption. The positive value of $\Delta S^o$ reveals an increase in randomness at the interface of solid-solution over the process of adsorption, which implies some extent structural changes of TC molecule and surface of *g*-$MoS_2$-BC (Zhao et al., 2011).

### 3.7 Adsorption mechanisms

Based on the above analysis, we speculate that multiple mechanisms and various interactions including non-specific and specific binding are involved in the whole TC adsorption process onto *g*-$MoS_2$-BC, as illustrated in Fig. 7. According to the discussion in the influences of pH on TC adsorption (inhibiting effect in acid and alkali solution caused by electrostatic repulsion), it is confirmed that the electrostatic force actually do exist. To shed light on more mechanisms of TC adsorption, the FT-IR spectrum (Fig. 3c) experiments of *g*-$MoS_2$-BC and TC-loaded *g*-$MoS_2$-BC were conducted and analyzed further. Carboxyl (–COOH) plays an important role in making the surface negatively charged, which is ascribed to its ionization. Upon adsorption treatment, the C–O stretching vibration peak at 2860 $cm^{-1}$ and C=O stretching peak at 1635 $cm^{-1}$ are observed by slightly shifting to 2863 and 1637 $cm^{-1}$, respectively. These changes of peak position might be caused by the deprotonation of carboxyl, confirming the existence of electrostatic interaction between TC and *g*-$MoS_2$-BC in adsorption process. Moreover, the stretching vibration peaks at 2368, 1635, 1446, 1095 $cm^{-1}$ derived from cumulated double bond, C=O, aromatic benzene ring skeleton, and C–O–C pyranose ring skeletal, respectively in composite occur in varying degrees of

migration, which can be attributed to the π-π conjugate effect with benzene ring, double bonds, amino and other functional groups of TC molecule as π electron donator or acceptor. Considering the graphene-like layered structure of *g*-$MoS_2$ and the four aromatic rings in TC molecular structure, the mechanism of π-π stacking interaction between aromatic compound TC and π electron-rich regions of *g*-$MoS_2$-BC composite is proposed as a crucial one. Besides, the adsorption peaks at 667 $cm^{-1}$ and around 3384-3450 $cm^{-1}$ designated to S–H and O–H vibration, respectively shift to lower absorbance areas after adsorption experiment, manifesting the existence of hydrogen bond between TC and *g*-$MoS_2$-BC, it proves that hydrogen-bonding interaction is also one of the mechanisms affecting the TC adsorption process. Moreover, owing to the hydrophobic microenvironment of *g*-$MoS_2$-BC surface accommodating TC molecules, it shows promoting effect on the hydrogen bonding by the large π subunit of condensed aromatic structure (Zhang et al., 2016). Furthermore, the *g*-$MoS_2$-BC composite is considered as a tailor-made adsorbent for TC removal due to the appropriate pore-size distribution, since the increasing mesoporous might decrease the steric hindrance effect and enhance adsorption (Tang et al., 2018). By comparing the pore-size distribution of *g*-$MoS_2$-BC surface before and after TC adsorption (Fig. 3a), the mesoporous in the range of 2-20 nm was found to be significantly reduced undergone the adsorption, suggesting the pore-filling by partition effect is also one of the mechanisms that influencing the adsorption process.

### 3.8 Application on real water samples and its recyclability

River water and tap water were used as the medium of TC solution to study the practical application of *g*-$MoS_2$-BC in complex aqueous system. It can be observed from the Fig. 5S, the adsorbed amount of TC by *g*-$MoS_2$-BC in river water and tap water are slightly higher than that in lab single system of deionized water. Because of the relatively low cationic concentration in the sampled water (Table 3S), the inhibitory effect is almost non-existent. The higher adsorption in the river water may be due to the wrapped and cross-linked of TC by the floccules or the additional adsorption by fine particles.

The recyclability of *g*-$MoS_2$-BC, an important indicator for assessing economy and applicability in large-scale application, was researched under three solution medium including deionized water, tap water and river water. It could be seen from Fig. 5S, regardless of the solution medium, the result describes a good recycle performance of *g*-$MoS_2$-BC with slight reduction after five cycles. After five adsorption/desorption cycles, the amount of adsorbed TC onto the recycled *g*-$MoS_2$-BC is about 163.07 mg/g in river water, which indicates the adsorbent still remains high adsorption capacity. Compared with other different adsorbents for TC adsorption (Table 4S), *g*-$MoS_2$-BC showed excellent performance in application and recyclability as well as the low-cost advantages, and it is considered as an adsorbent with great potential for removal of antibiotic contaminants from aquatic environment on a large scale application. Furthermore, the excellent catalytic ability of $MoS_2$ can be used to realize the regeneration of the saturated adsorbent by photo-degradation of loading TC molecules

under light irradiation, which is worthy of further study because no solid-liquid separation is required.

## 4. Conclusions

The novel biochar-based nanocomposite had been prepared by a facile hydrothermal synthesis and showed a considerable adsorbed amount of TC with appropriate pore structure and abundant oxygen-containing functional groups. The hierarchical $MoS_2$ nanomaterials were proved to be embedded in the biochar, and the modification did improve the adsorption performance of materials. The results indicated that the adsorption of TC onto *g*-$MoS_2$-BC is a spontaneous and endothermic multilayer formation course that following three-step process, and it is strongly dependent on contact time, pH, temperature and initial concentration. The binding mechanisms, including electrostatic interaction, pore-filling, hydrogen bonding, π-π interaction, and so on, are involved in the adsorption of TC molecules. Considering the cost-effective, high efficiency, excellent reusability and wide applicability, *g*-$MoS_2$-BC could be regard as a potential absorbent for removal the TC from polluted natural waters. Assembly of *g*-$MoS_2$ nanosheets onto biochar, a sustainable and reusable material, presents a wide range of possibilities for the further development of antibiotics-polluted water remediation without solid-liquid separation.

## Acknowledgments

This research was financially supported by the National Natural Science

Foundation of China (81773333, 51521006, 51479072, 51378190 and 51679082) and the Program for Changjiang Scholars and Innovative Research Team in University (IRT-13R17).

## References

Ahmed, M.B., Zhou, J.L., Ngo, H.H., Guo, W., Johir, M.A.H., Belhaj, D. 2017. Competitive sorption affinity of sulfonamides and chloramphenicol antibiotics toward functionalized biochar for water and wastewater treatment. *Bioresource Technology*, **238**, 306-312.

Berdinsky, A.S., Chadderton, L.T., Yoo, J.B., Gutakovsky, A.K., Fedorov, V.E., Mazalov, L.N., Fink, D. 2005. Structural changes of MoS2 nano-powder in dependence on the annealing temperature. *Applied Physics a-Materials Science & Processing*, **80**(1), 61-67.

Chang, K., Chen, W.X. 2011. L-Cysteine-Assisted Synthesis of Layered MoS2/Graphene Composites with Excellent Electrochemical Performances for Lithium Ion Batteries. *Acs Nano*, **5**(6), 4720-4728.

Chao, Y., Yang, L., Ji, H., Zhu, W., Pang, J., Han, C., Li, H. 2017. Graphene-analogue molybdenum disulfide for adsorptive removal of tetracycline from aqueous solution: equilibrium, kinetic, and thermodynamic studies. *Environmental Progress & Sustainable Energy*, **36**(3), 815-821.

Chao, Y., Zhu, W., Wu, X., Hou, F., Xun, S., Wu, P., Ji, H., Xu, H., Li, H. 2014. Application of graphene-like layered molybdenum disulfide and its excellent adsorption behavior for doxycycline antibiotic. *Chemical Engineering Journal*, **243**, 60-67.

Chen, M., Xu, P., Zeng, G.M., Yang, C.P., Huang, D.L., Zhang, J.C. 2015. Bioremediation of soils contaminated with polycyclic aromatic hydrocarbons,petroleum, pesticides,chlorophenols andheavymetalsby composting: Applications, microbes and future research needs. *Biotechnology Advances*, **33**(6), 745-755.

Cheng, M., Zeng, G.M., Huang, D.L., Lai, C., Xu, P., Zhang, C., Liu, Y. 2016. Hydroxyl radicals based advanced oxidation processes (AOPs) for remediation of soils contaminated with organic compounds: A review. *Chemical Engineering Journal*, **284**, 582–598.

Deng, J.H., Zhang, X.R., Zeng, G.M., Gong, J.L., Niu, Q.Y., Liang, J. 2013. Simultaneous removal of Cd(II) and ionic dyes from aqueous solution using magnetic graphene oxide nanocomposite as an adsorbent. *Chemical Engineering Journal*, **226**(8), 189-200.

Gong, J.L., Wang, B., Zeng, G.M., Yang, C.P., Niu, C.G., Niu, Q.Y., Zhou, W.J., Liang, Y. 2009. Removal of cationic dyes from aqueous solution using magnetic multi-wall carbon nanotube nanocomposite as adsorbent. *Journal of Hazardous Materials*, **164**(2-3), 1517-1522.

Han, S., Liu, K., Hu, L., Teng, F., Yu, P., Zhu, Y. 2017. Superior Adsorption and Regenerable Dye Adsorbent Based on Flower-Like Molybdenum Disulfide Nanostructure. *Science Report*, **7**, 43599.

Homem, V., Santos, L. 2011. Degradation and removal methods of antibiotics from aqueous matrices--a

review. *Journal Environmental Management*, **92**(10), 2304-47.

Jahangiri-Rad, M., Nadafi, K., Mesdaghinia, A., Nabizadeh, R., Younesian, M., Rafiee, M. 2013. Sequential study on reactive blue 29 dye removal from aqueous solution by peroxy acid and single wall carbon nanotubes: experiment and theory. *Iranian J Environ Health Sci Eng*, **10**(1), 5.

Ji, L.L., Chen, W., Duan, L., Zhu, D.Q. 2009. Mechanisms for strong adsorption of tetracycline to carbon nanotubes: A comparative study using activated carbon and graphite as adsorbents. *Environmental Science & Technology*, **43**(7), 2322-2327.

Kiran, V., Mukherjee, D., Jenjeti, R.N., Sampath, S. 2014. Active guests in the MoS2/MoSe2 host lattice: efficient hydrogen evolution using few-layer alloys of MoS2(1-x)Se2x. *Nanoscale*, **6**(21), 12856-12863.

Liang, J., Yang, Z., Tang, L., Zeng, G., Yu, M., Li, X., Wu, H., Qian, Y., Li, X., Luo, Y. 2017. Changes in heavy metal mobility and availability from contaminated wetland soil remediated with combined biochar-compost. *Chemosphere*, **181**, 281-288.

Liu, P.P., Wang, Q.R., Zheng, C.L. and He, C. 2017. Sorption of Sulfadiazine, Norfloxacin, Metronidazole, and Tetracycline by Granular Activated Carbon: Kinetics, Mechanisms, and Isotherms. *Water Air and Soil Pollution*, **228** (4), 129.

Liu, S., Xu, W.H., Liu, Y.G., Tan, X.F., Zeng, G.M., Li, X., Liang, J., Zhou, Z., Yan, Z.L., Cai, X.X. 2017. Facile synthesis of Cu(II) impregnated biochar with enhanced adsorption activity for the removal of doxycycline hydrochloride from water. *Science of the Total Environment*, **592**, 546-553.

Long, F., Gong, J.L., Zeng, G.M., Chen, L., Wang, X.Y., Deng, J.H., Niu, Q.Y., Zhang, H.Y., Zhang, X.R. 2011. Removal of phosphate from aqueous solution by magnetic Fe–Zr binary oxide. *Chemical Engineering Journal*, **171**(2), 448-455.

Qiao, X.Q., Hu, F.C., Tian, F.Y., Hou, D.F., Li, D.S. 2016. Equilibrium and kinetic studies on MB adsorption by ultrathin 2D MoS2 nanosheets. *Rsc Advances*, **6**(14), 11631-11636.

Qiao, X.Q., Zhang, Z.W., Tian, F.Y., Hou, D.F., Tian, Z.F., Li, D.S., Zhang, Q.C. 2017. Enhanced Catalytic Reduction of p-Nitrophenol on Ultrathin MoS2 Nanosheets Decorated with Noble Metal Nanoparticles. *Crystal Growth & Design*, **17**(6), 3538-3547.

Ren, X.Y., Zeng, G.M., Tang, L., Wang, J.J., Wan, J., Liu, Y.N., Yu, J.F., Yi, H., Ye, S.J., Deng, R. 2018. Sorption, transport and biodegradation - An insight into bioavailability of persistent organic pollutants in soil. *Science of the Total Environment*, **610**, 1154-1163.

Tan, X., Liu, S., Liu, Y., Gu, Y., Zeng, G., Cai, X., Yan, Z., Yang, C., Hu, X., Chen, B. 2016a. One-pot synthesis of carbon supported calcined-Mg/Al layered double hydroxides for antibiotic removal by slow pyrolysis of biomass waste. *Science Report*, **6**, 39691.

Tan, X., Liu, Y., Zeng, G., Wang, X., Hu, X., Gu, Y., Yang, Z. 2015. Application of biochar for the removal of pollutants from aqueous solutions. *Chemosphere*, **125**, 70-85.

Tan, X.F., Liu, Y.G., Gu, Y.L., Liu, S.B., Zeng, G.M., Cai, X., Hu, X.J., Wang, H., Liu, S.M., Jiang, L.H. 2016b. Biochar pyrolyzed from MgAl-layered double hydroxides pre-coated ramie biomass (Boehmeria nivea (L.) Gaud.): Characterization and application for crystal violet removal. *Journal Environmental Management*, **184**(Pt 1), 85-93.

Tang, L., Yu, J.F., Pang, Y., Zeng, G.M., Deng, Y.C., Wang, J.J., Ren, X.Y., Ye, S.J., Peng, B., Feng, H.P.

2018. Sustainable efficient adsorbent: alkali-acid modified magnetic biochar derived from sewage sludge for aqueous organic contaminant removal. *Chemical Engineering Journal*, **336**, 160-169.

Tang, W.W., Zeng, G.M., Gong, J.L., Liang, J., Xu, P., Zhang, C., Huang, B.B. 2014. Impact of humic/fulvic acid on the removal of heavy metals from aqueous solutions using nanomaterials: A review. *Science of the Total Environment*, **468**, 1014-1027.

Theerthagiri, J., Senthil, R.A., Senthilkumar, B., Reddy Polu, A., Madhavan, J., Ashokkumar, M. 2017. Recent advances in MoS 2 nanostructured materials for energy and environmental applications – A review. *Journal of Solid State Chemistry*, **252**, 43-71.

Tiwari, B., Sellamuthu, B., Ouarda, Y., Drogui, P., Tyagi, R.D., Buelna, G. 2017. Review on fate and mechanism of removal of pharmaceutical pollutants from wastewater using biological approach. *Bioresource Technology*, **224**, 1-12.

Vattikuti, S.V.P., Byon, C. 2016. Bi2S3 nanorods embedded with MoS2 nanosheets composite for photodegradation of phenol red under visible light irradiation. *Superlattices and Microstructures*, **100**, 514-525.

Voiry, D., Salehi, M., Silva, R., Fujita, T., Chen, M.W., Asefa, T., Shenoy, V.B., Eda, G., Chhowalla, M. 2013. Conducting MoS2 Nanosheets as Catalysts for Hydrogen Evolution Reaction. *Nano Letters*, **13**(12), 6222-6227.

Wan, J., Zeng, G., Huang, D., Hu, L., Xu, P., Huang, C., Deng, R., Xue, W., Lai, C., Zhou, C., Zheng, K., Ren, X., Gong, X. 2018. Rhamnolipid stabilized nanochlorapatite: Synthesis and enhancement effect on Pb-and Cd-immobilization in polluted sediment. *Journal of Hazardous Materials*, **343**, 332-339.

Wang, H., Wen, F., Chen, Y., Sun, T., Meng, H., Zhang, Y. 2016. Electrocatalytic determination of nitrite based on straw cellulose/molybdenum sulfide nanocomposite. *Biosensors & Bioelectronics*, **85**, 692-697.

Wang, J., Yang, Q., Zhang, L., Liu, M., Hu, N., Zhang, W., Zhu, W., Wang, R., Suo, Y., Wang, J. 2018. A hybrid monolithic column based on layered double hydroxide-alginate hydrogel for selective solid phase extraction of lead ions in food and water samples. *Food Chem*, **257**, 155-162.

Wang, X., Wang, A., Ma, J. 2017. Visible-light-driven photocatalytic removal of antibiotics by newly designed C3N4@MnFe2O4-graphene nanocomposites. *Journal of Hazardous Materials*, **336**, 81-92.

Wu, H.P., Lai, C., Zeng, G.M., Liang, J., Chen, J., Xu, J.J., Dai, J., Li, X.D., Liu, J.F., Chen, M., Lu, L.H., Hu, L., Wan, J. 2017. The interactions of composting and biochar and their implications for soil amendment and pollution remediation: a review. *Critical Reviews in Biotechnology*, **37**(6), 754-764.

Wu, Z., Zhong, H., Yuan, X., Wang, H., Wang, L., Chen, X., Zeng , G., Wu, Y. 2014. Adsorptive removal of methylene blue by rhamnolipid-functionalized graphene oxide from wastewater. *Water Research*, **2014**(67), 330-344.

Xu, P., Zeng, G.M., Huang, D.L., Lai, C., Zhao, M.H., Wei, Z., Li, N.J., Huang, C., Xie, G.X. 2012a. Adsorption of Pb(II) by iron oxide nanoparticles immobilized Phanerochaete chrysosporium : Equilibrium, kinetic, thermodynamic and mechanisms analysis. *Chemical Engineering Journal*, **203**(5), 423-431.

Xu, P., Zeng, G.M., Huang, D.L., Feng, C.L., Hu, S., Zhao, M.H., Lai, C., Wei, Z., Huang, C., Xie, G.X., Liu, Z.F. 2012b. Use of iron oxide nanomaterials in wastewater treatment: A review. *Science of the Total Environment*, **424**, 1-10.

Yang, L., Zheng, X., Liu, M., Luo, S., Luo, Y., Li, G. 2017a. Fast photoelectro-reduction of CrVI over MoS2@TiO2 nanotubes on Ti wire. *Journal of Hazardous Materials*, **329**, 230-240.

Yang, Q., Wang, Y., Wang, J., Liu, F., Hu, N., Pei, H., Yang, W., Li, Z., Suo, Y., Wang, J. 2018a. High effective adsorption/removal of illegal food dyes from contaminated aqueous solution by Zr-MOFs (UiO-67). *Food Chem*, **254**, 241-248.

Yang, Q.F., Wang, J., Chen, X.Y., Yang, W.X., Pei, H.N., Hu, N., Li, Z.H., Suo, Y.R., Li, T., Wang, J.L. 2018b. The simultaneous detection and removal of organophosphorus pesticides by a novel Zr-MOF based smart adsorbent. *Journal of Materials Chemistry A*, **6**(5), 2184-2192.

Yang, Q.F., Wang, J., Zhang, W.T., Liu, F.B., Yue, X.Y., Liu, Y.N., Yang, M., Li, Z.H., Wang, J.L. 2017b. Interface engineering of metal organic framework on graphene oxide with enhanced adsorption capacity for organophosphorus pesticide. *Chemical Engineering Journal*, **313**, 19-26.

Ye, S., Zeng, G., Wu, H., Zhang, C., Dai, J., Liang, J., Yu, J., Ren, X., Yi, H., Cheng, M., Zhang, C. 2017a. Biological technologies for the remediation of co-contaminated soil. *Critical Reviews in Biotechnology*, **37**(8), 1062-1076.

Ye, S.J., Zeng, G.M., Wu, H.P., Zhang, C., Liang, J., Dai, J., Liu, Z.F., Xiong, W.P., Wan, J., Xu, P.A., Cheng, M. 2017b. Co-occurrence and interactions of pollutants, and their impacts on soil remediation-A review. *Critical Reviews in Environmental Science and Technology*, **47**(16), 1528-1553.

Zeng, G., Wu, H., Liang, J., Guo, S., Hu, L., Xu, P., Liu, Y., Yuan, Y., He, X., He, Y. 2015. Efficiency of biochar and compost (or composting) combined amendments for reducing Cd, Cu, Zn and Pb bioavailability, mobility and ecological risk in wetland soil. *Rsc Advances*, **5**(44), 34541-34548.

Zhang, C., Lai, C., Zeng, G., Huang, D., Yang, C., Wang, Y., Zhou, Y., Cheng, M. 2016. Efficacy of carbonaceous nanocomposites for sorbing ionizable antibiotic sulfamethazine from aqueous solution. *Water Research*, **95**, 103-12.

Zhang, M., Gao, B., Yao, Y., Xue, Y., Inyang, M. 2012. Synthesis, characterization, and environmental implications of graphene-coated biochar. *Science of the Total Environment*, **435-436**, 567-72.

Zhang, Y., Zeng, G.M., Tang, L., Chen, J., Zhu, Y., He, X.X., He, Y. 2015. Electrochemical sensor based on electrodeposited graphene-Au modified electrode and nanoAu carrier amplified signal strategy for attomolar mercury detection. *Anal Chem*, **87**(2), 989-96.

Zhao, G.X., Li, J.X., Wang, X.K. 2011. Kinetic and thermodynamic study of 1-naphthol adsorption from aqueous solution to sulfonated graphene nanosheets. *Chemical Engineering Journal*, **173**(1), 185-190.

Zhao, Y., Zhang, X., Wang, C., Zhao, Y., Zhou, H., Li, J., Jin, H. 2017. The synthesis of hierarchical nanostructured MoS 2 /Graphene composites with enhanced visible-light photo-degradation property. *Applied Surface Science*, **412**, 207-213.

Zhou, C.Y., Lai, C., Huang, D.L., Zeng, G.M., Zhang, C., Cheng, M., Hu, L., Wan, J., Xiong, W.P., Wen, M., Wen, X.F., Qin, L. 2018. Highly porous carbon nitride by supramolecular preassembly of monomers for photocatalytic removal of sulfamethazine under visible light driven. *Applied Catalysis B-Environmental*, **220**, 202-210.

Zhou, W.J., Hou, D.M., Sang, Y.H., Yao, S.H., Zhou, J., Li, G.Q., Li, L.G., Liu, H., Chen, S.W. 2014. MoO2 nanobelts@nitrogen self-doped MoS2 nanosheets as effective electrocatalysts for hydrogen evolution reaction. *Journal of Materials Chemistry A*, **2**(29), 11358-11364.

Zhu, C., Zhang, L., Jiang, B., Zheng, J., Hu, P., Li, S., Wu, M., Wu, W. 2016. Fabrication of Z-scheme Ag 3 PO 4 /MoS 2 composites with enhanced photocatalytic activity and stability for organic pollutant degradation. *Applied Surface Science*, **377**, 99-108.

**Figure captions**

**Fig. 1** Schematic illustration of the formation of *g*-$MoS_2$-BC composite and its application for removal of TC

**Fig. 2** SEM images of pristine biochar (a), pure $MoS_2$ (b), *g*-$MoS_2$-BC (c), and $MoS_2$ sheets on *g*-$MoS_2$-BC composite (d), and HRTEM images of *g*-$MoS_2$-BC (e and f)

**Fig. 3** (a) The pore-size distribution curve of *g*-$MoS_2$-BC and TC-loaded *g*-$MoS_2$-BC, inset shows $N_2$ adsorption-desorption isotherms of *g*-$MoS_2$-BC at 77 K; (b) XRD patterns of pure $MoS_2$, *g*-$MoS_2$-BC and TC-loaded *g*-$MoS_2$-BC; (c) FT-IR spectrums of pure $MoS_2$, *g*-$MoS_2$-BC and TC-loaded *g*-$MoS_2$-BC, (d) XPS survey spectra of pristine biochar and *g*-$MoS_2$-BC

**Fig. 4** The XPS spectra of *g*-$MoS_2$-BC composite: high resolution XPS spectrum of Mo 3d and S 2s (a), S 2p (b), C 1s (c), and O 1s (d)

**Fig. 5** (a) Zeta potentials of *g*-$MoS_2$-BC at different pH ranging from 2.0-11.0 and the effect of pH values, (b) effect of ionic strength on adsorption capacity of *g*-$MoS_2$-BC for TC. Error bars represent standard error of the mean (n=3). Different letters indicate significant difference ($p<0.05$) between each salt concentration.

**Fig. 6** Effect of contact time on the adsorption of TC onto *g*-$MoS_2$-BC (a); the pseudo-first-order plots (b), pseudo-second-order plots (c), intra-particle diffusion plots (d), Boyd plots (e) and Bangham plots (f) for TC adsorption by *g*-$MoS_2$-BC

**Fig. 7** The proposed mechanisms for the removal behavior of TC onto *g*-$MoS_2$-BC

**Table 1 Adsorption kinetics parameters of pseudo-first-order kinetic, pseudo-second-order kinetic and Bangham model for TC on *g*-$MoS_2$-BC**

| Concentration (mg/L) | Pseudo-first-order kinetic | | | | Pseudo-second-order kinetic | | | Bangham model | | |
|---|---|---|---|---|---|---|---|---|---|---|
| | $q_{e,exp}$ (mg/g) | $k_1$ (1/h) | $q_{e,cal}$ (mg/g) | $R^2$ | $k_2$ (g/mg.h) | $q_{e,cal}$ (mg/g) | $R^2$ | $k_B$ | m | $R^2$ |
| **50** | 103.676 | 0.002303 | 31.225 | 0.9428 | 0.000465 | 104.167 | 0.9994 | 49.957 | 9.560 | 0.9672 |
| **100** | 174.285 | 0.002763 | 58.144 | 0.9448 | 0.000248 | 175.438 | 0.9993 | 83.714 | 9.701 | 0.9876 |
| **150** | 208.583 | 0.002994 | 66.911 | 0.9807 | 0.000203 | 209.643 | 0.9992 | 113.083 | 11.936 | 0.9927 |

**Table 2 The obtained parameters' value of intra-particle and Boyd's film-diffusion models**

| Kinetics models | Parameters | | Initial concentration (mg/L) | | |
|---|---|---|---|---|---|
| | | | 50 | 100 | 150 |
| **Intra-particle diffusion** | $K_{id}$ $(mg/g{\bullet}min^{1/2})$ | $K_{1d}$ | 4.986 | 5.403 | 4.738 |
| | | $K_{2d}$ | 1.225 | 2.316 | 2.058 |
| | | $K_{3d}$ | 0.244 | 0.516 | 0.484 |
| | $C_i$ | $C_1$ | 45.502 | 87.822 | 122.691 |
| | | $C_2$ | 69.932 | 111.834 | 146.113 |
| | | $C_3$ | 93.766 | 153.521 | 188.554 |
| | $R_i^2$ | $R_1^2$ | 0.9694 | 0.9580 | 0.9831 |
| | | $R_2^2$ | 0.9524 | 0.9691 | 0.9854 |
| | | $R_3^2$ | 0.8063 | 0.8691 | 0.9425 |
| **Boyd's film-diffusion** | $R_i^2$ | $R_1^2$ | 0.9468 | 0.9724 | 0.9702 |
| | | $R_2^2$ | 0.9947 | 0.9673 | 0.9771 |

**Table 3 The obtained results of isotherm models for TC adsorption**

| Isotherm models | Parameters | Temperature (K) | | |
|---|---|---|---|---|
| | | 298 | *308* | *318* |
| **Langmuir** | $R^2$ | 0.9927 | 0.9919 | 0.9913 |
| | $K_L$ *(L/mg)* | 0.0553 | 0.0637 | 0.0887 |
| | $q_{max}$ *(mg/g)* | 249.376 | 423.728 | 699.301 |
| | $R_L$ | 0.0692 | 0.0803 | 0.1017 |
| **BET model** | $R^2$ | 0.9981 | 0.9953 | 0.9928 |
| | $K_b$ | 4430.910 | 3202.787 | 2782.223 |
| | $q_{max}$ *(mg/g)* | 248.561 | 422.385 | 696.492 |
| **Freundlich** | $R^2$ | 0.9473 | 0.9745 | 0.9772 |
| | $K_F$ *(L/mg)* | 30.372 | 40.988 | 64.508 |
| | *1/n* | 0.447 | 0.497 | 0.529 |
| **Temkin** | $R^2$ | 0.9651 | 0.9358 | 0.9169 |
| | $K_T$ *(L/mg)* | 73.402 | 136.687 | 142.263 |
| | $B_T$ | 30.154 | 40.119 | 51.088 |
| | $b_T$ *(J/mol)* | 82.246 | 63.889 | 57.799 |
| **D-R model** | $R^2$ | 0.8138 | 0.7713 | 0.7604 |
| | *E (kJ/mol)* | 0.863 | 0.992 | 1.107 |
| | $q_{max}$ *(mg/g)* | 168.891 | 243.464 | 315.977 |

**Fig. 1**

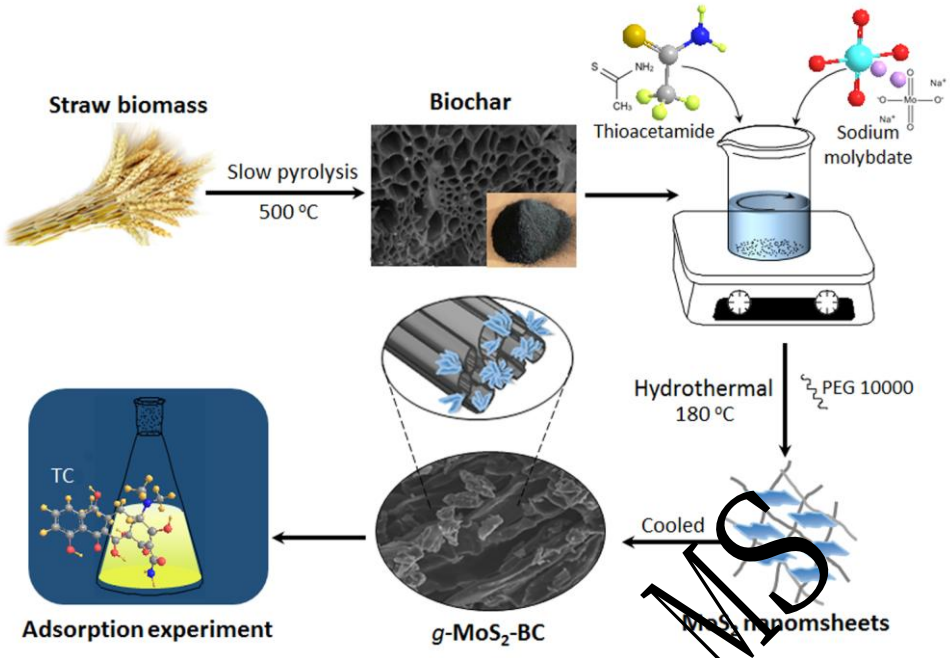

**Fig. 2**

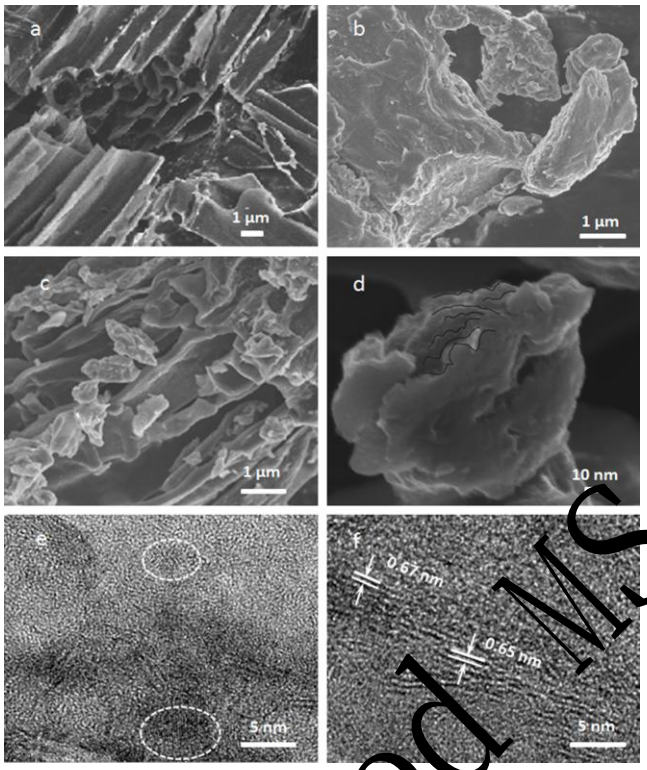

**Fig. 3**

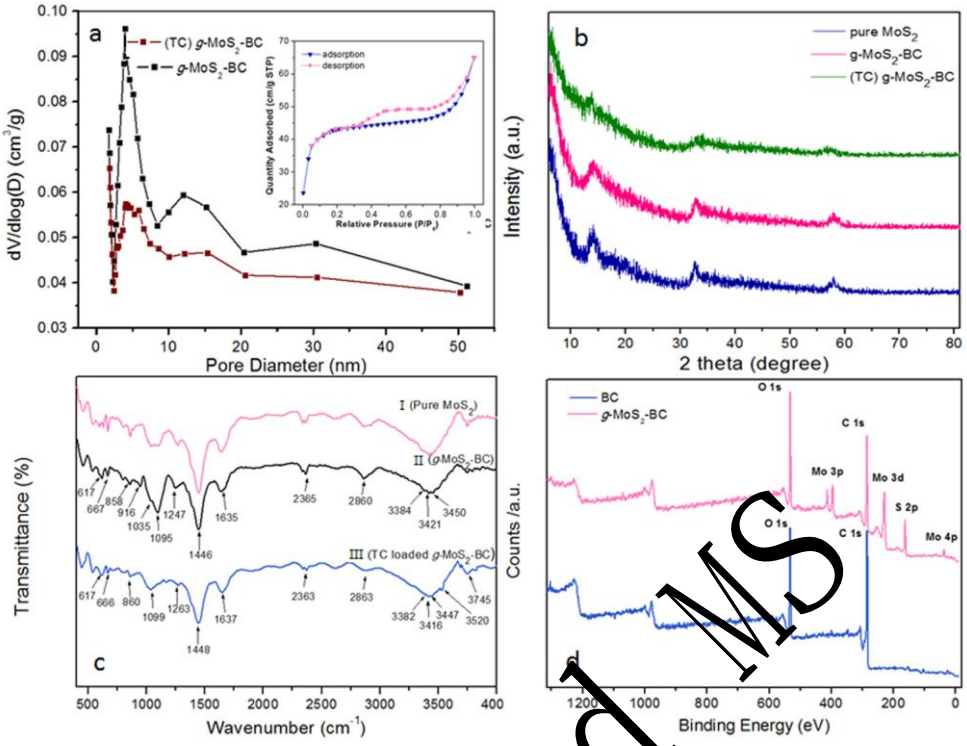

**Fig. 4**

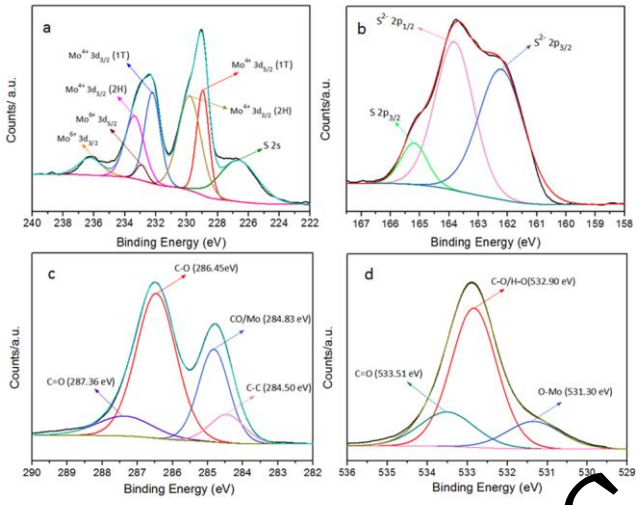

**Fig. 5**

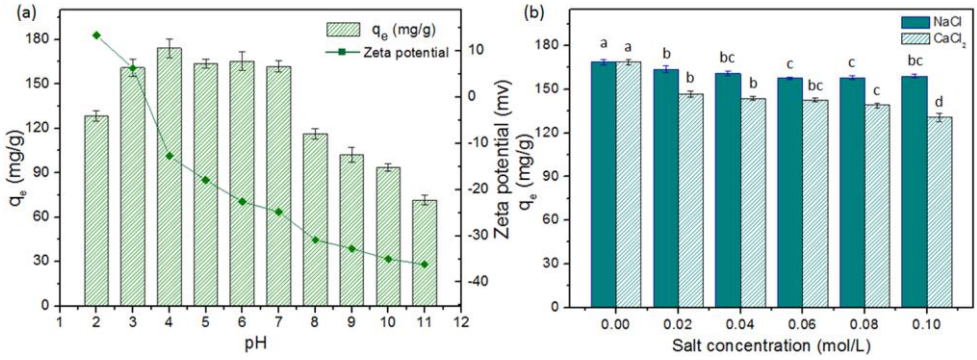

**Fig. 6**

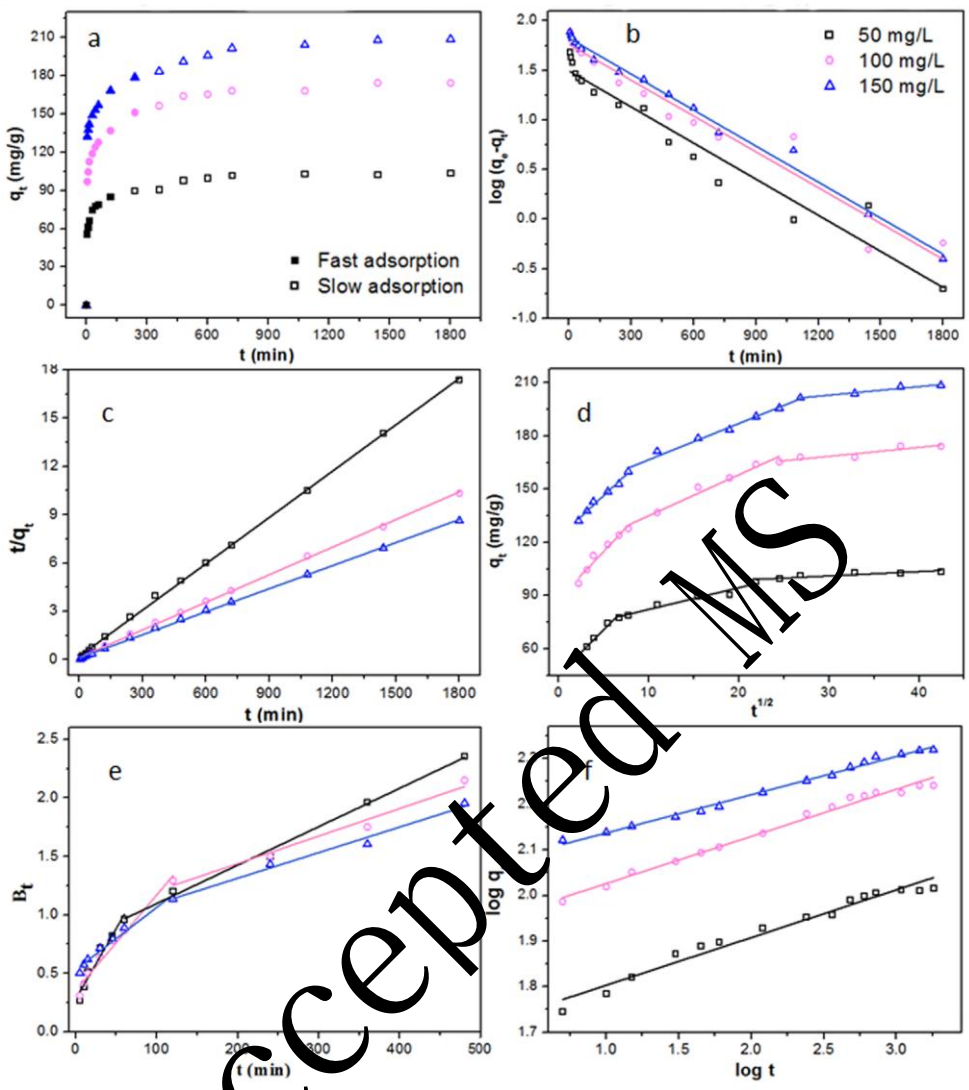

**Fig. 7**

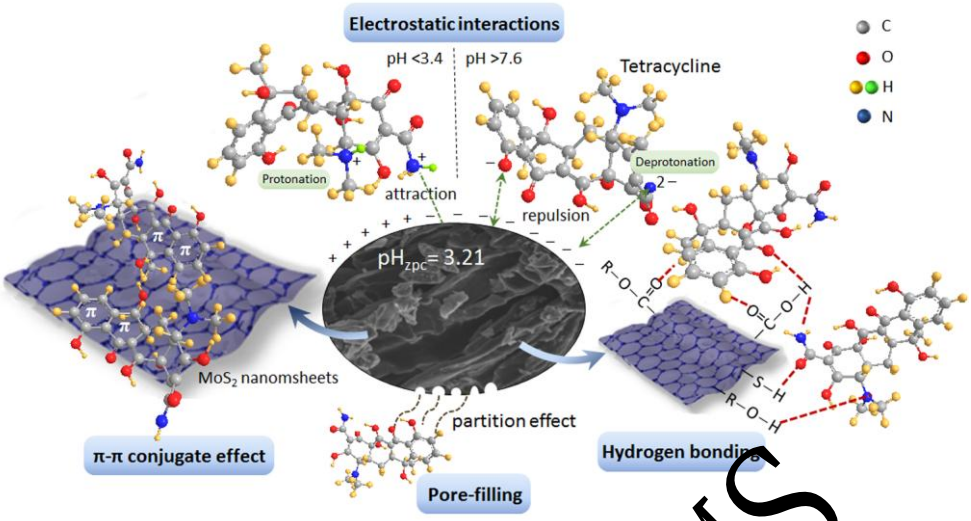

***Graphical Abstract**

Graphical abstract

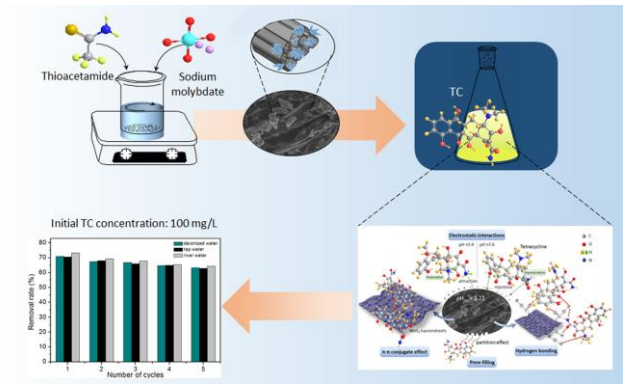

*Highlights (for review : 3 to 5 bullet points (maximum 85 characters including spaces per bullet point)

**Highlights**

- Hierarchical *g*-$MoS_2$ nanosheets were successfully loaded onto the surface of biochar.
- Pore structures and surface properties of biochar were improved by decorated with *g*-$MoS_2$.
- Sustainable efficient removal for TC by novel *g*-$MoS_2$-biochar nanocomposite was confirmed.
- Several mechanisms participated in the antibiotic removal were also discussed.
- Further research focuses on the catalytic degradation ability of nanocomposite for its regeneration.

# Research on the sustainable efficacy of *g*-$MoS_2$ decorated biochar nanocomposites for removing tetracycline hydrochloride from antibiotic-polluted aqueous solution

Zhuotong Zeng [a, 1], Shujing Ye [b, 1], Haipeng Wu [a, b, c, 1], Rong Xiao [a,*], Guangming Zeng [a, b,*], Jie Liang [b], Chang Zhang [b], Jiangfang Yu [b], Yilong Fang [b], Biao Song [b]

[a] Department of Dermatology, Second Xiangya Hospital, Central South University, Changsha 410011, P R China

[b] College of Environmental Science and Engineering, Hunan University and Key Laboratory of Environmental Biology and Pollution Control (Hunan University), Ministry of Education, Changsha 410082, P.R. China

[c] Changjiang River Scientific Research Institute, Wuhan 430010, PR China



[*] Corresponding authors: Tel.: +86–731–88822754; fax: +86–731–88823701. Email address: xiaorong65@csu.edu.cn (Rong Xiao) and zgming@hnu.edu.cn (Guangming Zeng).

[1] These authors contribute equally to this article.

**ABSTRACT**

Antibiotic concentrations in surface waters far exceed the pollution limit due to the abuse of pharmaceuticals, resulting in an urgent need for an approach with potential efficiency, sustainability and eco-friendliness to remove antibiotic pollutants. A novel biochar-based nanomaterial was synthesized by hydrothermal synthesis and was investigated for its removal potential for tetracycline hydrochloride (TC) from both artificial and real wastewater. The associative facilitation between biochar and *g*-$MoS_2$ nanosheets was proposed, revealing the favorable surface structures and adsorption properties of the composite. The related adsorption kinetics, isotherms and thermodynamics were studied by several models with adsorption experimental data, turning out that biochar decorated by *g*-$MoS_2$ exhibited optimum TC removal with adsorption capacity up to 249.45 mg/g at 298 K. The adsorption behavior of TC molecules on *g*-$MoS_2$-BC can be interpreted well by three-step process, and it is dominated by several mechanisms containing pore-filling, electrostatic force, hydrogen bond and π-π interaction. In addition, the cost-effective *g*-$MoS_2$-BC nanocomposites demonstrated excellent adsorption and recycling performance in TC-contaminated river water, which might provide the underlying insights needed to guide the design of promising approach for contaminant removal on a large scale in practical application.

**Keywords**: Biochar-based nanocomposite; *g*-$MoS_2$; Tetracycline hydrochloride; Sustainable application; Removal mechanisms

## 1. Introduction

Antibiotics, as emerging pollutants, are released into the environment in large quantities due to abuse of pharmaceuticals, and they have been detected excessively in surface water, ground water and sediment (Chao et al., 2014; Zhou et al., 2018). The existence of antibiotic residues in the environment has caused high concern because of their potential long-term adverse threats on human health and natural ecosystem (Ren et al., 2018; Ye et al., 2017b). There is an increasing demand for the removal of antibiotics from contaminated water to avoid the ecological risk. A growing number of researches have been explored for the remediation of antibiotics-contaminated water (Tiwari et al., 2017), containing biotechnology (degrading microorganism) (Chen et al., 2015; Ye et al., 2017a), chemical technology (oxidation, photo-catalysis) (Cheng et al., 2016; Wang et al., 2017) and physical technology (separation) (Gong et al., 2009; Wan et al., 2018; Xu et al., 2012b). However, some deficiencies restrict the application of these technologies, for instance, the growth-restricted microorganisms as for biological processes; high energy/cost consumption and toxic by-products as for chemical processes; and low efficiency as for pure physical separation (Ahmed et al., 2017; Tang et al., 2014). Tetracycline hydrochloride (TC) with amphoteric behavior, a kind of widely used antimicrobial, has been detected frequently in aquatic ecosystems, and it is difficult to degrade even with more toxic byproducts (Homem & Santos, 2011). Adsorption is a way that affects the migration-transformation of antibiotics in the aquatic environment, which is considered as a feasible and economical approach for

antibiotic removal (Chao et al., 2017; Liu et al., 2017).

Adsorbents play an important role in polluted water remediation, some common adsorbents and their modifications have been studied for removal of antibiotics from aqueous solution, such as graphene (Deng et al., 2013; Yang et al., 2017b), clay minerals (Long et al., 2011; Xu et al., 2012a), metal organic framework (Wang et al., 2018; Yang et al., 2018a, b), carbon nanotubes (Ji et al., 2009; Zhang et al., 2015) and powder activated carbon (Liu et al. 2017). Among them, biochar shows excellent adsorption performance as well as carbon sequestration based on its favorable physico-chemical surface characteristics, like high hydrophobicity and aromaticity, large surface area and developed pore structure (Liu et al., 2017; Ye et al., 2017a). Moreover, biochar is more environmentally and economically viable, since it is derived from the pyrolysis of waste biomass, allowing the resources recovery and utilization (Liang et al., 2017; Wu et al., 2017; Zeng et al., 2015). However, the effectiveness of biochar relies heavily on the temperatures and raw materials of production. In order to get better removal efficiency for pollutants, biochar is modified by metallic embedding, nanomaterial decorating and surface functionalization based on various mechanisms (Tan et al., 2015; Ye et al., 2017b). Zhang et al. (2012) prepared an engineered graphene-coated biochar, and the results showed the adsorbed amount of contaminant on the graphene-coated biochar was enhanced by the strong π-π interaction between aromatic structure of pollutant molecules and graphene sheets on biochar surface, which was more than 20 times higher than that of the pristine biochar (Zhang et al.,

2012). It is still a challenge to develop a cost-effective adsorbent for water treatment on large scale application, along with the difficulties in separation and regeneration of used adsorbent.

Molybdenum disulfide with a special layered structure (*g*-$MoS_2$) is a novel quasi-two-dimensional lamellar nanomaterial similar to graphene, which had been proposed as a potential alternative for removal of antibiotics (Chao et al., 2017; Chao et al., 2014; Han et al., 2017; Theerthagiri et al., 2017). A $MoS_2$ molecule possesses the S-Mo-S sandwich structure with the Mo atom sandwiched between two S atoms. Due to the large surface area, surface covalent forces and strong edge effects (Kiran et al., 2014), the researches of *g*-$MoS_2$ in contaminant adsorption (Chao et al., 2014; Qiao et al., 2016), electrochemical performance (Voiry et al., 2013; Wang et al., 2016), and catalytic degradation (Vattikuti & Byon, 2016; Zhu et al., 2016), etc. have drawn huge deal of scientific interests. However, *g*-$MoS_2$ nanosheets have relatively low dispersibility and tend to agglomerate, thereby adversely affecting the remediation efficiency as well as having bad impacts on aquatic organisms. Until now, no systematic study concerning the adsorption performance of $MoS_2$ nanomaterial-decorated biochar (biochar is used as substrate and is modified to a nanocomposite with *g*-$MoS_2$ nanosheets) in antibiotic removal from aquatic environment has been published yet.

In this work, a novel adsorbent of *g*-$MoS_2$ nanosheet-decorated biochar (*g*-$MoS_2$-BC) was synthesized firstly using a facile hydrothermal method. Batch

adsorption experiments were designed to investigate the adsorption performance of the composite in aqueous solution that contaminated with tetracycline hydrochloride (TC). The main aims of the research were to 1) synthesize and characterize the *g*-$MoS_2$-BC; 2) explore the adsorption behavior of TC on surface of *g*-$MoS_2$-BC, including the adsorption kinetics, isotherms, thermodynamics, mechanisms as well as the factors potentially affecting the adsorbed amount; and 3) investigate the removal efficiency of *g*-$MoS_2$-BC applied in real TC wastewater.

## 2. Materials and methods

### 2.1. Materials

Rice straw was obtained from bottomland of Dongting Lake, located in Changsha, China. Tetracycline hydrochloride (TC, purity >98.5%), sodium molybdate and thioacetamide were purchased from Shanghai Chemical Corp and used without purification. Besides, deionized water (18.25 MΩ/cm) used in the experiment was produced by an Ulupure (UPRII-10 T) laboratory water system.

### 2.2 Preparation of *g*-$MoS_2$-decorated biochar

As shown in Fig. 1, biochar was produced by slow pyrolysis of agricultural straw in tube furnace operating at a continuous flow of $N_2$ gas and a temperature of 500 °C for a residence time of 2 h, according to previous research (Zeng et al., 2015). In a typical synthesis of the $MoS_2$ nanosheets, 230 mg of $Na_2MoO_4 \cdot 2H_2O$ and 460 mg of thioacetamide were dissolved in 60 mL deionized water, in which 0.1 g of the prepared biochar and 0.1 mM PEG10000 were added in sequence with magnetic stirring, and the

mixture dispersed via ultrasonication for 30 min. Afterwards, the whole solution was transferred to a 100 mL Teflon-lined autoclave and heated up to 180 °C for 24 h by hydrothermal treatment. After the mixture was cooled to room temperature naturally, the black solid precipitate (*g*-$MoS_2$-BC) produced in the solution was collected by centrifugation (8000 rpm for 5 min), and then was washed six times with anhydrous ethanol and deionized water, thereby drying in an oven at 80 °C for overnight.

2.3. Characterization methods

The field emission scanning electron microscope (SEM, JSM-6700F, Japan) equipped with an energy dispersive X-ray analyzer (EDS, AMETER, USA) was used to examine the surface morphology and elemental compositions of the *g*-$MoS_2$-BC. The structural details of the composite were further characterized by the transmission electron microscopy (TEM). The BET specific surface area and pore characteristics were calculated based on the $N_2$ adsorption-desorption isotherms at 77.3 K by using automatic surface and porosity analyzer (Quantachrome, USA). Fourier transform infrared spectrum (FT-IR) measurements, recorded in the range of 4000-400 $cm^{-1}$, were performed in KBr pellet by Nicolet 5700 Spectrometer, USA. The X-ray diffraction (XRD) patterns were showed by Bruker AXS D8 Advance diffractometer equipping with a Cu-K*a* radiation source (λ=1.5417 Å) to explore the crystal structures of as-synthesized composite. Binding energies of the material elements were conducted based on the X-ray photoelectron spectroscopy (XPS, Thermo Fisher Scientific-K-Alpha 1063, UK), with the calibration of C1s at 284.8 eV.

Thermogravimetric analysis (TGA) was carried out under nitrogen flow with a heating rate of 10 °C/min (TG209, Netzsch, Shanghai, China). The zeta potentials analysis of *g*-$MoS_2$-BC and TC were determined using Electroacoustic Spectrometer (ZEN3600 Zetasizer, UK) at solution pH ranging from 2.0 to 11.0.

2.4. Adsorption and removal of TC by *g*-$MoS_2$-BC

The batch experiments were carried out in 100 mL Erlenmeyer flasks containing the mixture of 20 mg *g*-$MoS_2$-BC and 50 mL TC aqueous solution. All flasks were wrapped with aluminum foils to avoid photodegradation and then placed in a thermostatic water shaking bath at an agitation speed of 150 rpm. The desired pH of solution were achieved by the adjustment with 0.1 M NaOH or 0.1 M HCl measured by pH meter (PHSJ-5, China), varying from 2.0 to 11.0 in initial TC solution (100 mg/L). The effect of salt ionic strength on the removal of TC (100 mg/L) was studied with the sodium chloride (NaCl) and calcium chloride ($CaCl_2$) at concentration range of 0-0.1 M. After shaking under 298 K for 24 h, the samples were taken from the flasks, followed by centrifuged and filtered using 0.45 μm PVDF disposable filters prior to UV spectrophotometry (UV-2550, SHIMADZU, Japan) at $\lambda_{max}$ 357 nm.

Adsorption kinetics studies were carried out by mixing 20 mg of as-synthesized composite and 50 mL TC solution with initial concentration of 50, 100, 150 mg/L at pH of 4.0. The solution was shaken with a speed of 150 rpm at temperature of 298 K, and samples were taken at predetermined time intervals (from 5 min to 30 h) for the determination of TC residual concentration after filtration. Adsorption isotherm and

thermodynamic experiments of *g*-$MoS_2$-BC were performed under three different temperatures (298, 308, and 318 K). 50 mL TC solutions with different initial concentrations ranging from 10 to 400 mg/L were adjusted to pH at 4.0 and then mixed with 20 mg composite for shaking. The TC concentrations of sample were then determined by above-mentioned ultraviolet spectrophotometry method after centrifugation and filtration.

The research on practical application of *g*-$MoS_2$-BC in real water samples (river water: obtained from Xiang River located in Changsha for TC solution preparation without filtration) was conducted by mixing 20 mg of *g*-$MoS_2$-BC with 50 mL real wastewater polluted by TC (100 mg/L), and the mixture was shaken at 298 K for 24 h. The regeneration of *g*-$MoS_2$-BC was carried out by adding TC-loaded *g*-$MoS_2$-BC to 50 mL NaOH (0.2 mol/L) and stirring the mixture at temperature of 298 K and agitation speed of 140 r/min for 24 h. The suspension liquid was centrifuged after desorption, and the collected solid (regenerated *g*-$MoS_2$-BC) was dried at 353 K and applied for next round of adsorption experiment with four-times repetition.

## 3. Results and discussion

### 3.1 Characterization of *g*-$MoS_2$-BC composite

The surface morphologies and micro-structures of the manufactured materials were examined by SEM and TEM. The SEM image of pristine biochar (Fig. 2a) shows essentially the smooth surface morphology composing of closely packed tubular structures with a cavity size of 1-2 μm. Upon the modification, the resulting

*g*-$MoS_2$-BC composite was found to be relatively uneven surface decorated with $MoS_2$ stacking hierarchical structure. A high magnification SEM image of the composite, presented in Fig. 2c, reveals that the tubular carbon material is disorderly assembled by crumpled nanosheets with curved edges, indicating the biochar could be regarded as a fresh substrate for supporting hierarchical $MoS_2$ nanosheets. The interactions between the oxygen-containing functional groups of biochar and $Mo^{4+}$ precursors might be responsible for the *in situ* growth of $MoS_2$ nanosheets on biochar surface (Chang & Chen, 2011; Zhao et al., 2017). Compared with the bulk structure of pure $MoS_2$ (Fig. 2b), the $MoS_2$ in composite (Fig. 2d) exhibits cluster framework with relatively few layers stacking, which is conducive to the exposure of active sites with defect-rich structure. The TEM images (Fig. S2) and HRTEM (Fig. e and f) further confirm a hierarchical crumpled and disordered structure with curved edges onto the carbon-based materials. HRTEM image illustrates the discontinued fringes of the curled edges, indicating the defect-rich structure with ample surface sites (Qiao et al., 2017). The lattice fringes of *g*-$MoS_2$ on composite display interplanar spacing of ~ 0.67 nm, the different interlayer distances should be associated with the intercalation of $MoS_2$ nanosheets and biochar.

In order to examine the porous properties of *g*-$MoS_2$-BC composite, Brunauer-Emmett-Teller (BET) gas sorptometry measurement was conducted. The inset of Fig. 3a describes the $N_2$ adsorption/desorption isotherm of the composite, which can be identified as type IV isotherm with a hysteresis loop, demonstrating the

mesoporous characteristic of *g*-$MoS_2$-BC. The observed large hysteresis loop is intermediate between typical H3- and H4-type isotherm, which is considered to be derived from the stack of laminated layered structure of the slit pore. The corresponding pore-size distribution, obtained from the isotherm by using the BJH method and shown in Fig. 3a, elucidates that most of the pores fall into the size range of 2 to 20 nm and the average pore diameter is calculated to be 3.509 nm. It is well established that adsorbent might exhibit the best adsorption performance when its pore diameter is 1.7-3 times larger than the adsorbate molecular size (even more than 3-6 times if adsorbent needs to be recycled) (Tang et al., 2018). Taking the TC molecule dimension (1.41 nm long, 0.46 nm wide and 0.82 nm high) into account, we conclude that *g*-$MoS_2$-BC composite is endowed with adsorption capacity for efficient TC molecular removal based on their pore-size distribution. On the whole, the prepared composite exhibits a BET specific surface area of 176.8 $m^2/g$ and a pore volume of 0.0839 $cm^3/g$. Both are higher than the corresponding value of the pristine biochar, it should be noted that the change could be attributed to the extra mosaic structure of $MoS_2$ nanosheets with plenty of folded edges like wings.

The X-ray powder diffraction (XRD) patterns of the as-prepared $MoS_2$ and *g*-$MoS_2$-BC composite are shown in Fig. 3b. The three detected diffraction peaks are indexed to (002), (100) and (110) planes, respectively, indicating a hexagonal phase of $MoS_2$ (JCPDS card No. 37–1492) (Chao et al., 2014). Subtle changes in the peak location may be due to the strain effect by bending of the layers or lattice expansion

introduced by crystal defects (Berdinsky et al., 2005). Especially, the (002) diffraction peak, resulted primarily from the scattering of interlayer Mo–Mo (Yang et al., 2017a), is feeble in the pattern, suggesting that $MoS_2$ is consisted of only a few layers nanosheets. There is no obvious difference in peak position between pure $MoS_2$ and the *g*-$MoS_2$-BC composite due to the low XRD intensity of biochar, which also reveals that the chemical composition of $MoS_2$ has not changed after the surface modification. From the variation in width and strength of (002) plane diffraction peak, it can be observed that the growth of $MoS_2$ crystal along the *c*-axis in composite is inhibited owing to the presence of biochar, demonstrating fewer stack of $MoS_2$ layers.

FT-IR analysis was carried out to investigate the surface property of the BC and *g*-$MoS_2$-BC composite. It can be seen from the Fig. 3c, several characteristic FT-IR peaks of biochar are observed in composite, including 3384-3450 $cm^{-1}$ for O–H stretching, 2860 $cm^{-1}$ for C–O of carboxyl, 2365 $cm^{-1}$ for cumulated double bonds stretching, 1635 $cm^{-1}$ for C=C vibration, 1446 $cm^{-1}$ for aromatic benzene ring skeletal vibration, 1247 $cm^{-1}$ for C–O stretching, 1039 and 1095 $cm^{-1}$ for C–O–C pyranose ring skeletal vibration, 858 $cm^{-1}$ for C–H bending vibrations and 667 $cm^{-1}$ for S–H vibration. In addition to the common functional groups above mentioned, a new stretch at 617 $cm^{-1}$ appearing in curve (II) is assigned to $\gamma_{as}$ Mo–S vibration (Wang et al., 2016), demonstrating the successful bindidng of $MoS_2$ onto the biochar surface. Moreover, another fresh peak presenting at 916 $cm^{-1}$ in curve (II) could be ascribed to the stretching vibration of Mo=O (Han et al., 2017), which implies the partial oxidation

of the Mo atom on edge of nanosheet. Curve (III) in the Fig. 3c describes the FT-IR spectrum of TC-loaded *g*-$MoS_2$-BC, the enhanced and broadened peaks approximately at 3500 to 3900 $cm^{-1}$ are probably originated from the extra functional groups of TC molecule, especially the peak around 3520 $cm^{-1}$ corresponding to the acylamino of TC. These observations confirmed that the TC molecules are successfully adsorbed on the surface of *g*-$MoS_2$-BC composite.

X-ray photoelectron spectroscopy (XPS) was performed to further investigate the surface chemical composition and valence state of the elements in *g*-$MoS_2$-BC composite. The survey spectrum, presented in Fig. 3d, reveals the *g*-$MoS_2$-BC composite is composed of four major elements of C, O, Mo, and S. Compared with the biochar before and after modification, besides the introduction of Mo, and S elements in *g*-$MoS_2$-BC, the proportion of oxygen in the element composition is observed to increase, which implies that more oxygen-containing functional groups appear on composite surface. In the high resolution XPS spectrum of Mo 3d, shown in Fig. 4a, two peaks locating at 232.30 eV and 229.00 eV can be assigned to Mo $3d_{3/2}$ and Mo $3d_{5/2}$, respectively, characterizing of $Mo^{4+}$ in 1T-$MoS_2$, while the doublet peaks presenting at about 233.28 and 229.76 eV are attributed to the $3d_{3/2}$ and $3d_{5/2}$ of $Mo^{4+}$ in 2H–$MoS_2$ (Qiao et al., 2016). Meanwhile, two weak peaks centering at 236.17 and 232.90 eV are attributed to the oxidation state $Mo^{6+}$, which might be derived from the slight oxidation of Mo atoms at the defect or edges of $MoS_2$ nanosheets due to the high oxidation activity (Zhou et al., 2014). The peaks at 163.80 and 162.20 eV (Fig. 4b)

could be indexed to S 2p1/2 and S 2p3/2 orbital of divalent sulfide, respectively, suggesting the valence state of S element is -2. In combination with another analysis of peak at 226.66 eV (Fig. 4a) arising from S 2s, the existence of $MoS_2$ on the composite is confirmed. In the C 1s XPS spectrum (Fig. 4c) of composite, the C 1s band is deconvoluted into four peaks locating at 284.50, 284.83, 286.45, and 287.36 eV, assigning to the binding of C=C/C–C, CO/Mo, C–O and C=O, respectively. The binding energies of O 1s peaks (Fig. 4d) are observed at about 532.90, 531.30 and 533.51 eV, corresponding to the O–C/O–H, O–Mo and O=C, respectively, which are consistent with the FT-IR results.

The thermal stability of the prepared materials was examined by TGA which is shown in Fig. S3. The weight percentage of both materials was observed to decrease with increasing temperature from 20 to 800 °C. Compared with the pristine biochar, modified biochar has considerably high thermal stability before 450 °C with an approximate 5% weight loss. However, the weight percentage of *g*-$MoS_2$-BC dropped sharply after 500 °C, which could be attributed to the decomposition of the loaded $MoS_2$ and organic species that adsorbed on material surface during synthesis process.

**3.2 Effect of pH on TC adsorption**

It is generally believed that pH plays an important role in influencing adsorption capacity by changing both surface properties of adsorbent and adsorbate. The effect of solution pH varying from 2.0 to 11.0 on TC adsorption to *g*-$MoS_2$-BC was investigated, and the corresponding results with the zeta potential of *g*-$MoS_2$-BC are measured and

illustrated in Fig. 5a. It could be observed that the adsorption capacity exhibits increasing trend when pH value changes from 2.0 to 4.0, but the effect is little when pH value in the range of 5.0-7.0, sequentially, the declining trend of adsorption capacity is obvious especially when pH value >8.0.

The surface charge of *g*-$MoS_2$-BC, which makes great influences on the adsorption process of TC, is sensitive to the solution pH value. According to the result obtained by Fig. 5a, the zero potential point ($pH_{ZPC}$) of *g*-$MoS_2$-BC is around 3.21, the adsorbent surface shows electronegative and decreases gradually with increasing pH value when $pH>pH_{ZPC}$, owing to the dissociation of carboxylic group on the surface of *g*-$MoS_2$-BC. Besides the charge change of adsorbent surface, the chemical speciation of organic compound also transforms by the protonation/deprotonation transition of functional groups at different pH (Tan et al., 2016a). Tetracycline is amphoteric molecule along with multiple ionizable functional groups, which exists cations ($TCH_3^+$: derived from protonation of the dimethyl-ammonium group), zwitterions ($TCH_2^0$: derived from deprotonation of the phenolic diketone moiety), and anions ($TCH^-$ and $TC^{2-}$: derived from deprotonation of the tri-carbonyl groups and phenolic diketone moiety) in accordance with the different dissociation constant ($pK_a$=3.4, 7.6 and 9.7) (Chao et al., 2017). When the pH value is below 3.21, both surface Zeta potential of TC and *g*-$MoS_2$-BC composite are positive and decrease with the increasing pH value of the solution, demonstrating the weakening effect of the electrostatic repulsion which is favorable for adsorption. TC is predominantly existed as zwitterion at pH values

ranging of 4.0-7.0 with almost no net electrical charge, resulting in little electrostatic interactions (attraction or repulsion) and unobvious effect of pH changing on the adsorption capacity. The comparatively large adsorption capacity at pH in this range may be determined by other interactions, such as hydrogen bond, π-π and hydrophobic interaction (Chao et al., 2017), as will be described below. Nevertheless, when pH value is >8, the negatively charged surface of *g*-$MoS_2$-BC is generally decreases and presents an enhancing electrostatic repulsion to anions $TCH^-$ and $TC^{2-}$, which adversely affects the adsorbed amount of TC.

**3.3 Effect of ionic strength on the adsorption capacity**

In order to get closer to the actual situation of natural water, different amounts of sodium chloride and calcium chloride ranging from 0-0.1 mol/L were added to solution to explore the influences of ionic strength on the adsorption capacity. As can be seen from Fig. 5b, the addition of extra ions slightly decreases the adsorbed amount of TC in generally, while the adsorption capacity changes very little with the increasing NaCl concentration. There are two possible reasons accounted for the slight change: (1) equalizing effect: on one hand, the $Na^+$ ions inhibit the electrostatic interaction between the TC cations with *g*-$MoS_2$-BC groups by competition (Wu et al., 2014); on the other hand, the salt would be beneficial for the dissociation of TC molecules to $TC^+$ by facilitating the protonation and result in promoting electrostatic interaction (Tan et al., 2016b). And (2) electrostatic interaction is only a considerably weak mechanism that affects the adsorption of TC on *g*-$MoS_2$-BC. However, the downtrend is evident

and it represents obvious inhibiting effect of TC adsorption with the increase of $CaCl_2$ concentration. This difference may arise from much higher screening effect by $CaCl_2$ on the electrostatic interaction compared with NaCl, and thus more actives sites are occupied by $Ca^{2+}$, which confirms the electrostatic interaction has a certain degree in the domination of adsorption.

### 3.4 Effect of time and adsorption kinetics

As shown in Fig. 6a, the adsorption of TC by *g*-$MoS_2$-BC is a time-dependent process, which could be divided into two phases: fast- and slow- adsorption stages. Attributed to the abundant active sites and attractive electrostatic force on composite surface for TC molecules, it is found that the adsorbed amount increased as the increasing contact time, and nearly 85% of the adsorption capacity was accomplished within the first 4 h, which is defined as fast-adsorption stages. Then, the adsorption was performed at much lower rate. The adsorption rate went down gradually until there was no significant variation in the adsorbed amount after 24 h, which represents that the adsorption equilibrium has been achieved.

In order to further analyze the kinetics of TC adsorption onto *g*-$MoS_2$-BC, the experimental data were fitted by pseudo-first-order, pseudo-second-order, intra-particle diffusion, Boyd's film-diffusion and Bangham channel diffusion models at three different initial TC concentrations to research the characteristics of the adsorption process in this study. The linear forms of these kinetic models are presented in Table S1, and the related kinetic parameters calculated by linear regression are summarized in

Table 1 and Table 2.

The pseudo-first-order and pseudo-second-order models are two universal model widely used for investigation of the adsorption kinetics. Compared with the pseudo-first-order model, pseudo-second-order model is more consistent with the adsorption behavior across the whole experimental on the basis of the significant higher values of correlation coefficient (Table 1). This is also supported by the favorable fitting between the equilibrium adsorption capacity obtained from experimental data ($q_{e,exp}$) and the calculated values ($q_{e,cal}$) in pseudo-second-order model, suggesting the adsorption behavior is much affected by chemical mechanism. It should also be mentioned that the pseudo-second-order rate constants ($k_2$) reduces with increasing initial TC concentration, which could be attributed to the low competition of TC molecules for adsorption sites at lower initial concentration.

To achieve a better understanding of the diffusion mechanisms and possible rate controlling adsorption process, Intra-particle diffusion, Boyd's film-diffusion and Bangham channel diffusion model were further applied. Intra-particle diffusion model, an empirically functional relationship of adsorbed amount, is used to analyze experimental data with some crucial parameters (intra-particle diffusion rate constant $k_{id}$, and $C_i$ related to the thickness of boundary layer). As can be seen from part d of Fig. 6, the plots of $q_t$ against $t^{1/2}$ are consisted of three linear sections, indicating that the TC adsorption processes are associated with multiple steps. High linear correlation coefficient and all non-zero $C_i$ values, presented in Table 2, imply that intra-particle

diffusion is involved in the adsorption process, while it is not the only rate-controlling step (Wu et al., 2014). The first linear section with a relatively sharp slope demonstrates the transport of TC from bulk solution to the external surface of *g*-$MoS_2$-BC, which is controlled by the molecule diffusion and film diffusion. The second section with slow slope describes the gradual adsorption stage, where the intra-particle diffusion dominates, that is, the diffusion of the TC molecules transfer into the pores of *g*-$MoS_2$-BC from its external surface. The last linear section with tardy slope implies the arrival of adsorption equilibrium. Comparing the rate constant of three stages, $k_{1d}$ is much larger than other two values, indicating that the film diffusion of TC molecules transferring through the boundary liquid layer is the most important limiting step of the adsorption. The wing-like *g*-$MoS_2$ with a quasi-two-dimensional few-layered structure, embedded in the biochar surface, helps TC molecules reach the active sites of surface more easily, since the TC molecules only need to divert from liquid phase through the boundary liquid membrane, but barely need to transfer in limited intermediate layer (Chao et al., 2017).

To shed light on the actual rate-controlling step participated in the overall TC adsorption process, the Boyd's film-diffusion and Bangham channel diffusion model were used to illustrate the experimental data. On the basis of these models, the linearity of the plots provides the fairly reliable information to define the actual rate-controlling step as film diffusion or intra-particle diffusion. The plots of calculated $B_t$ versus time t for early stage of first 8 h are the segment-line which do not pass through the origin,

suggesting that the rate-controlling step is dominated by film diffusion at the initial stage of adsorption process, subsequently took over by other mechanisms (intra-particle diffusion). Furthermore, the relatively good linear coefficients of Bangham channel diffusion model, presented in Table 1, reveal the performance of channel diffusion behavior in this adsorption process. In general, the adsorption of TC onto the surface of *g*-$MoS_2$-BC includes three steps: (1) the TC molecules overcome the liquid resistance and transfer from the solution phase to the exterior surface of *g*-$MoS_2$-BC controlled by film diffusion; (2) the TC molecules migrate on the surface and enter the pores of particles, as the adsorbent particles are loaded with TC; and (3) the TC molecules that arrived at the active site are absorbed on the interior surface of *g*-$MoS_2$-BC and gradually reach the adsorption equilibrium.

**3.5 Adsorption isotherms**

The isotherm plays an important role in designing the adsorption system, which shows the distribution of solute molecules in solution phase and solid phase upon adsorption reaching equilibrium. The relationship between the equilibrium adsorption capacity ($q_e$) and equilibrium TC concentration ($C_e$) in solution, presented in Fig. S4a, shows the adsorption capacity of *g*-$MoS_2$-BC enhances with increasing initial TC concentration in the range of 10-400 mg/L. This may be explained by the more powerful driving force provided by higher initial TC concentration to overcome the mass transfer resistances between aqueous and solid phases (Qiao et al., 2016). To further explore the isotherms, the adsorption equilibrium data at temperature of 298,

308, and 318 K were fitted by different equilibrium models including Langmuir, Freundlich, Temkin, BET isotherm and Dubinin-Redushckevich (D-R) isotherm models. The forms of these isotherm models and their related isotherm parameters are presented in Table S1 and Table 3, respectively.

The Langmuir model, based on the assumption of monolayer adsorption on specific homogenous sites without interactions between molecules, is shown in the Fig. S4b. The linear relation is obtained from $C_e/q_e$ against $C_e$ with highest correlation coefficients, revealing that the adsorption of TC onto *g*-$MoS_2$-BC probably is monolayer molecular adsorption associated with the functions of chemical mechanism. Concerning the different temperature, the parameters $q_{max}$ and $k_L$ increases as temperature rises up, implying higher temperature is likely to inspire adsorption through enhancing the bond energy between TC molecules and surface sites (Tang et al., 2018). It is noteworthy that a critical characteristic, the dimensionless constant separation factor $R_L$, is found to be between 0 and 1, which suggests that the adsorption process is favorable. As an improvement of the Langmuir model, the BET adsorption isotherm model is based on the assumption that the adsorbates are randomly adsorbed on a homogeneous surface to form a multi-molecular layer without horizontal interaction. The TC adsorption equilibrium data is fitted better by BET model (inset of Fig. S4b) with higher correlation coefficient (Table 3), demonstrating the adsorption on *g*-$MoS_2$-BC surface may be multilayer formation (Jahangiri-Rad et al., 2013).

Freundlich model is an empirical formula which assumes that there are multilayers

of adsorbate on heterogeneous surface. It can fit the experimental data well as indicated by the good correlation coefficients ($R^2$ > 0.948), suggesting that the physical interaction also takes part in the TC adsorption on *g*-$MoS_2$-BC surface. The $K_F$ value, represented the adsorption capacity, was observed to increase with the increasing temperature. An essential parameter, heterogeneity factor *1/n*, is used to describe the bond distribution, and all *1/n* values are less than 1, suggesting the adsorption is facile and favorable at all tested temperature. On the whole, the adsorption behavior of TC molecular onto the *g*-$MoS_2$-BC surface is determined by the combined impacts of the physical and chemical mechanisms.

In contrast to the models mentioned above, the Temkin isotherm model assumes that the adsorption heat of the adsorbate on the surface decreases linearly with increasing coverage, which is closer to the actual state of the adsorption experiment. As shown in Fig. S4d, the linear regression plot of $q_e$ versus $lnC_e$ is relatively weak observed by the correlation coefficients ($R^2$) in range of 0.915-0.965, which reveals that the chemical mechanism is not the only controlled interaction for the TC adsorption behavior. This is consistent with the calculated values of $b_T$ (related to the heat of adsorption) in Table 3, since the low $b_T$ value reflects the comparatively weak chemical interaction between TC molecules and surface of *g*-$MoS_2$-BC (Wu et al., 2014). Finally, the D-R isotherm model was also analyzed in its linearized form regarding to the TC concentration at equilibrium. The calculated sorption free energy values (*E*) shown in Table 3 are lower than 8, confirming the occurrence of physical

adsorption behavior of TC molecular. However, given the relatively small correlation coefficient, the physical driving force is considered to have a limited role in TC adsorption process.

### 3.6 Thermodynamic analysis

As can be seen from part a of Fig. S4, temperature is observed to have a significant effect on TC adsorption behavior. The adsorption capacity improves obviously with the increasing temperature, and the average adsorption capacity increases from 174.701 mg/g at 298 K to 226.653 mg/g at 318 K with about 30% rises under initial TC concentration of 100 mg/L, which suggests that the adsorption is an endothermic process. High temperature is favorable for adsorption, due to the swelling effect on the particle porosity which makes the pore volume allow TC molecules to rapidly diffuse through the external boundary layer and within interior pore of *g*-$MoS_2$-BC. The adsorption of TC under different temperature was investigated to make clear the thermodynamic property. Related parameters containing the Gibbs free energy ($\Delta G^o$), enthalpy ($\Delta H^o$), and entropy ($\Delta S^o$) were determined by Gibbs-Helmholtz equation. All negative values of $\Delta G^o$, shown in Table S2, confirm that the absorption process of TC molecules on *g*-$MoS_2$-BC surface is spontaneous and feasible, and it is observed to decrease from -4.649 kJ/mol to -9.129 kJ/mol as the temperature increasing, manifesting that the adsorption is more favorable at higher temperature. The $\Delta G^o$ value is in the range of -20~0 kJ/mol, confirming again the role of physical interactions in this adsorption process. Based on the positive value of $\Delta H^o$, we prove

the endothermic nature of TC adsorption. The positive value of $\Delta S^o$ reveals an increase in randomness at the interface of solid-solution over the process of adsorption, which implies some extent structural changes of TC molecule and surface of *g*-$MoS_2$-BC (Zhao et al., 2011).

### 3.7 Adsorption mechanisms

Based on the above analysis, we speculate that multiple mechanisms and various interactions including non-specific and specific binding are involved in the whole TC adsorption process onto *g*-$MoS_2$-BC, as illustrated in Fig. 7. According to the discussion in the influences of pH on TC adsorption (inhibiting effect in acid and alkali solution caused by electrostatic repulsion), it is confirmed that the electrostatic force actually do exist. To shed light on more mechanisms of TC adsorption, the FT-IR spectrum (Fig. 3c) experiments of *g*-$MoS_2$-BC and TC-loaded *g*-$MoS_2$-BC were conducted and analyzed further. Carboxyl (–COOH) plays an important role in making the surface negatively charged, which is ascribed to its ionization. Upon adsorption treatment, the C–O stretching vibration peak at 2860 $cm^{-1}$ and C=O stretching peak at 1635 $cm^{-1}$ are observed by slightly shifting to 2863 and 1637 $cm^{-1}$, respectively. These changes of peak position might be caused by the deprotonation of carboxyl, confirming the existence of electrostatic interaction between TC and *g*-$MoS_2$-BC in adsorption process. Moreover, the stretching vibration peaks at 2368, 1635, 1446, 1095 $cm^{-1}$ derived from cumulated double bond, C=O, aromatic benzene ring skeleton, and C–O–C pyranose ring skeletal, respectively in composite occur in varying degrees of

migration, which can be attributed to the π-π conjugate effect with benzene ring, double bonds, amino and other functional groups of TC molecule as π electron donator or acceptor. Considering the graphene-like layered structure of *g*-$MoS_2$ and the four aromatic rings in TC molecular structure, the mechanism of π-π stacking interaction between aromatic compound TC and π electron-rich regions of *g*-$MoS_2$-BC composite is proposed as a crucial one. Besides, the adsorption peaks at 667 $cm^{-1}$ and around 3384-3450 $cm^{-1}$ designated to S–H and O–H vibration, respectively shift to lower absorbance areas after adsorption experiment, manifesting the existence of hydrogen bond between TC and *g*-$MoS_2$-BC, it proves that hydrogen-bonding interaction is also one of the mechanisms affecting the TC adsorption process. Moreover, owing to the hydrophobic microenvironment of *g*-$MoS_2$-BC surface accommodating TC molecules, it shows promoting effect on the hydrogen bonding by the large π subunit of condensed aromatic structure (Zhang et al., 2016). Furthermore, the *g*-$MoS_2$-BC composite is considered as a tailor-made adsorbent for TC removal due to the appropriate pore-size distribution, since the increasing mesoporous might decrease the steric hindrance effect and enhance adsorption (Tang et al., 2018). By comparing the pore-size distribution of *g*-$MoS_2$-BC surface before and after TC adsorption (Fig. 3a), the mesoporous in the range of 2-20 nm was found to be significantly reduced undergone the adsorption, suggesting the pore-filling by partition effect is also one of the mechanisms that influencing the adsorption process.

### 3.8 Application on real water samples and its recyclability

River water and tap water were used as the medium of TC solution to study the practical application of *g*-$MoS_2$-BC in complex aqueous system. It can be observed from the Fig. 5S, the adsorbed amount of TC by *g*-$MoS_2$-BC in river water and tap water are slightly higher than that in lab single system of deionized water. Because of the relatively low cationic concentration in the sampled water (Table 3S), the inhibitory effect is almost non-existent. The higher adsorption in the river water may be due to the wrapped and cross-linked of TC by the floccules or the additional adsorption by fine particles.

The recyclability of *g*-$MoS_2$-BC, an important indicator for assessing economy and applicability in large-scale application, was researched under three solution medium including deionized water, tap water and river water. It could be seen from Fig. 5S, regardless of the solution medium, the result describes a good recycle performance of *g*-$MoS_2$-BC with slight reduction after five cycles. After five adsorption/desorption cycles, the amount of adsorbed TC onto the recycled *g*-$MoS_2$-BC is about 163.07 mg/g in river water, which indicates the adsorbent still remains high adsorption capacity. Compared with other different adsorbents for TC adsorption (Table 4S), *g*-$MoS_2$-BC showed excellent performance in application and recyclability as well as the low-cost advantages, and it is considered as an adsorbent with great potential for removal of antibiotic contaminants from aquatic environment on a large scale application. Furthermore, the excellent catalytic ability of $MoS_2$ can be used to realize the regeneration of the saturated adsorbent by photo-degradation of loading TC molecules

under light irradiation, which is worthy of further study because no solid-liquid separation is required.

## 4. Conclusions

The novel biochar-based nanocomposite had been prepared by a facile hydrothermal synthesis and showed a considerable adsorbed amount of TC with appropriate pore structure and abundant oxygen-containing functional groups. The hierarchical $MoS_2$ nanomaterials were proved to be embedded in the biochar, and the modification did improve the adsorption performance of materials. The results indicated that the adsorption of TC onto *g*-$MoS_2$-BC is a spontaneous and endothermic multilayer formation course that following three-step process, and it is strongly dependent on contact time, pH, temperature and initial concentration. The binding mechanisms, including electrostatic interaction, pore-filling, hydrogen bonding, π-π interaction, and so on, are involved in the adsorption of TC molecules. Considering the cost-effective, high efficiency, excellent reusability and wide applicability, *g*-$MoS_2$-BC could be regard as a potential absorbent for removal the TC from polluted natural waters. Assembly of *g*-$MoS_2$ nanosheets onto biochar, a sustainable and reusable material, presents a wide range of possibilities for the further development of antibiotics-polluted water remediation without solid-liquid separation.

## Acknowledgments

This research was financially supported by the National Natural Science

Foundation of China (81773333, 51521006, 51479072, 51378190 and 51679082) and the Program for Changjiang Scholars and Innovative Research Team in University (IRT-13R17).

## References

Ahmed, M.B., Zhou, J.L., Ngo, H.H., Guo, W., Johir, M.A.H., Belhaj, D. 2017. Competitive sorption affinity of sulfonamides and chloramphenicol antibiotics toward functionalized biochar for water and wastewater treatment. *Bioresource Technology*, **238**, 306-312.

Berdinsky, A.S., Chadderton, L.T., Yoo, J.B., Gutakovsky, A.K., Fedorov, V.E., Mazalov, L.N., Fink, D. 2005. Structural changes of MoS2 nano-powder in dependence on the annealing temperature. *Applied Physics a-Materials Science & Processing*, **80**(1), 61-67.

Chang, K., Chen, W.X. 2011. L-Cysteine-Assisted Synthesis of Layered MoS2/Graphene Composites with Excellent Electrochemical Performances for Lithium Ion Batteries. *Acs Nano*, **5**(6), 4720-4728.

Chao, Y., Yang, L., Ji, H., Zhu, W., Pang, J., Han, C., Li, H. 2017. Graphene-analogue molybdenum disulfide for adsorptive removal of tetracycline from aqueous solution: equilibrium, kinetic, and thermodynamic studies. *Environmental Progress & Sustainable Energy*, **36**(3), 815-821.

Chao, Y., Zhu, W., Wu, X., Hou, F., Xun, S., Wu, P., Ji, H., Xu, H., Li, H. 2014. Application of graphene-like layered molybdenum disulfide and its excellent adsorption behavior for doxycycline antibiotic. *Chemical Engineering Journal*, **243**, 60-67.

Chen, M., Xu, P., Zeng, G.M., Yang, C.P., Huang, D.L., Zhang, J.C. 2015. Bioremediation of soils contaminated with polycyclic aromatic hydrocarbons,petroleum, pesticides,chlorophenols andheavymetalsby composting: Applications, microbes and future research needs. *Biotechnology Advances*, **33**(6), 745-755.

Cheng, M., Zeng, G.M., Huang, D.L., Lai, C., Xu, P., Zhang, C., Liu, Y. 2016. Hydroxyl radicals based advanced oxidation processes (AOPs) for remediation of soils contaminated with organic compounds: A review. *Chemical Engineering Journal*, **284**, 582–598.

Deng, J.H., Zhang, X.R., Zeng, G.M., Gong, J.L., Niu, Q.Y., Liang, J. 2013. Simultaneous removal of Cd(II) and ionic dyes from aqueous solution using magnetic graphene oxide nanocomposite as an adsorbent. *Chemical Engineering Journal*, **226**(8), 189-200.

Gong, J.L., Wang, B., Zeng, G.M., Yang, C.P., Niu, C.G., Niu, Q.Y., Zhou, W.J., Liang, Y. 2009. Removal of cationic dyes from aqueous solution using magnetic multi-wall carbon nanotube nanocomposite as adsorbent. *Journal of Hazardous Materials*, **164**(2-3), 1517-1522.

Han, S., Liu, K., Hu, L., Teng, F., Yu, P., Zhu, Y. 2017. Superior Adsorption and Regenerable Dye Adsorbent Based on Flower-Like Molybdenum Disulfide Nanostructure. *Science Report*, **7**, 43599.

Homem, V., Santos, L. 2011. Degradation and removal methods of antibiotics from aqueous matrices--a

review. *Journal Environmental Management*, **92**(10), 2304-47.

Jahangiri-Rad, M., Nadafi, K., Mesdaghinia, A., Nabizadeh, R., Younesian, M., Rafiee, M. 2013. Sequential study on reactive blue 29 dye removal from aqueous solution by peroxy acid and single wall carbon nanotubes: experiment and theory. *Iranian J Environ Health Sci Eng*, **10**(1), 5.

Ji, L.L., Chen, W., Duan, L., Zhu, D.Q. 2009. Mechanisms for strong adsorption of tetracycline to carbon nanotubes: A comparative study using activated carbon and graphite as adsorbents. *Environmental Science & Technology*, **43**(7), 2322-2327.

Kiran, V., Mukherjee, D., Jenjeti, R.N., Sampath, S. 2014. Active guests in the MoS2/MoSe2 host lattice: efficient hydrogen evolution using few-layer alloys of MoS2(1-x)Se2x. *Nanoscale*, **6**(21), 12856-12863.

Liang, J., Yang, Z., Tang, L., Zeng, G., Yu, M., Li, X., Wu, H., Qian, Y., Li, X., Luo, Y. 2017. Changes in heavy metal mobility and availability from contaminated wetland soil remediated with combined biochar-compost. *Chemosphere*, **181**, 281-288.

Liu, P.P., Wang, Q.R., Zheng, C.L. and He, C. 2017. Sorption of Sulfadiazine, Norfloxacin, Metronidazole, and Tetracycline by Granular Activated Carbon: Kinetics, Mechanisms, and Isotherms. *Water Air and Soil Pollution*, **228** (4), 129.

Liu, S., Xu, W.H., Liu, Y.G., Tan, X.F., Zeng, G.M., Li, X., Liang, J., Zhou, Z., Yan, Z.L., Cai, X.X. 2017. Facile synthesis of Cu(II) impregnated biochar with enhanced adsorption activity for the removal of doxycycline hydrochloride from water. *Science of the Total Environment*, **592**, 546-553.

Long, F., Gong, J.L., Zeng, G.M., Chen, L., Wang, X.Y., Deng, J.H., Niu, Q.Y., Zhang, H.Y., Zhang, X.R. 2011. Removal of phosphate from aqueous solution by magnetic Fe–Zr binary oxide. *Chemical Engineering Journal*, **171**(2), 448-455.

Qiao, X.Q., Hu, F.C., Tian, F.Y., Hou, D.F., Li, D.S. 2016. Equilibrium and kinetic studies on MB adsorption by ultrathin 2D MoS2 nanosheets. *Rsc Advances*, **6**(14), 11631-11636.

Qiao, X.Q., Zhang, Z.W., Tian, F.Y., Hou, D.F., Tian, Z.F., Li, D.S., Zhang, Q.C. 2017. Enhanced Catalytic Reduction of p-Nitrophenol on Ultrathin MoS2 Nanosheets Decorated with Noble Metal Nanoparticles. *Crystal Growth & Design*, **17**(6), 3538-3547.

Ren, X.Y., Zeng, G.M., Tang, L., Wang, J.J., Wan, J., Liu, Y.N., Yu, J.F., Yi, H., Ye, S.J., Deng, R. 2018. Sorption, transport and biodegradation - An insight into bioavailability of persistent organic pollutants in soil. *Science of the Total Environment*, **610**, 1154-1163.

Tan, X., Liu, S., Liu, Y., Gu, Y., Zeng, G., Cai, X., Yan, Z., Yang, C., Hu, X., Chen, B. 2016a. One-pot synthesis of carbon supported calcined-Mg/Al layered double hydroxides for antibiotic removal by slow pyrolysis of biomass waste. *Science Report*, **6**, 39691.

Tan, X., Liu, Y., Zeng, G., Wang, X., Hu, X., Gu, Y., Yang, Z. 2015. Application of biochar for the removal of pollutants from aqueous solutions. *Chemosphere*, **125**, 70-85.

Tan, X.F., Liu, Y.G., Gu, Y.L., Liu, S.B., Zeng, G.M., Cai, X., Hu, X.J., Wang, H., Liu, S.M., Jiang, L.H. 2016b. Biochar pyrolyzed from MgAl-layered double hydroxides pre-coated ramie biomass (Boehmeria nivea (L.) Gaud.): Characterization and application for crystal violet removal. *Journal Environmental Management*, **184**(Pt 1), 85-93.

Tang, L., Yu, J.F., Pang, Y., Zeng, G.M., Deng, Y.C., Wang, J.J., Ren, X.Y., Ye, S.J., Peng, B., Feng, H.P.

2018. Sustainable efficient adsorbent: alkali-acid modified magnetic biochar derived from sewage sludge for aqueous organic contaminant removal. *Chemical Engineering Journal*, **336**, 160-169.

Tang, W.W., Zeng, G.M., Gong, J.L., Liang, J., Xu, P., Zhang, C., Huang, B.B. 2014. Impact of humic/fulvic acid on the removal of heavy metals from aqueous solutions using nanomaterials: A review. *Science of the Total Environment*, **468**, 1014-1027.

Theerthagiri, J., Senthil, R.A., Senthilkumar, B., Reddy Polu, A., Madhavan, J., Ashokkumar, M. 2017. Recent advances in MoS 2 nanostructured materials for energy and environmental applications – A review. *Journal of Solid State Chemistry*, **252**, 43-71.

Tiwari, B., Sellamuthu, B., Ouarda, Y., Drogui, P., Tyagi, R.D., Buelna, G. 2017. Review on fate and mechanism of removal of pharmaceutical pollutants from wastewater using biological approach. *Bioresource Technology*, **224**, 1-12.

Vattikuti, S.V.P., Byon, C. 2016. Bi2S3 nanorods embedded with MoS2 nanosheets composite for photodegradation of phenol red under visible light irradiation. *Superlattices and Microstructures*, **100**, 514-525.

Voiry, D., Salehi, M., Silva, R., Fujita, T., Chen, M.W., Asefa, T., Shenoy, V.B., Eda, G., Chhowalla, M. 2013. Conducting MoS2 Nanosheets as Catalysts for Hydrogen Evolution Reaction. *Nano Letters*, **13**(12), 6222-6227.

Wan, J., Zeng, G., Huang, D., Hu, L., Xu, P., Huang, C., Deng, R., Xue, W., Lai, C., Zhou, C., Zheng, K., Ren, X., Gong, X. 2018. Rhamnolipid stabilized nanochlorapatite: Synthesis and enhancement effect on Pb-and Cd-immobilization in polluted sediment. *Journal of Hazardous Materials*, **343**, 332-339.

Wang, H., Wen, F., Chen, Y., Sun, T., Meng, H., Zhang, Y. 2016. Electrocatalytic determination of nitrite based on straw cellulose/molybdenum sulfide nanocomposite. *Biosensors & Bioelectronics*, **85**, 692-697.

Wang, J., Yang, Q., Zhang, L., Liu, M., Hu, N., Zhang, W., Zhu, W., Wang, R., Suo, Y., Wang, J. 2018. A hybrid monolithic column based on layered double hydroxide-alginate hydrogel for selective solid phase extraction of lead ions in food and water samples. *Food Chem*, **257**, 155-162.

Wang, X., Wang, A., Ma, J. 2017. Visible-light-driven photocatalytic removal of antibiotics by newly designed C3N4@MnFe2O4-graphene nanocomposites. *Journal of Hazardous Materials*, **336**, 81-92.

Wu, H.P., Lai, C., Zeng, G.M., Liang, J., Chen, J., Xu, J.J., Dai, J., Li, X.D., Liu, J.F., Chen, M., Lu, L.H., Hu, L., Wan, J. 2017. The interactions of composting and biochar and their implications for soil amendment and pollution remediation: a review. *Critical Reviews in Biotechnology*, **37**(6), 754-764.

Wu, Z., Zhong, H., Yuan, X., Wang, H., Wang, L., Chen, X., Zeng , G., Wu, Y. 2014. Adsorptive removal of methylene blue by rhamnolipid-functionalized graphene oxide from wastewater. *Water Research*, **2014**(67), 330-344.

Xu, P., Zeng, G.M., Huang, D.L., Lai, C., Zhao, M.H., Wei, Z., Li, N.J., Huang, C., Xie, G.X. 2012a. Adsorption of Pb(II) by iron oxide nanoparticles immobilized Phanerochaete chrysosporium : Equilibrium, kinetic, thermodynamic and mechanisms analysis. *Chemical Engineering Journal*, **203**(5), 423-431.

Xu, P., Zeng, G.M., Huang, D.L., Feng, C.L., Hu, S., Zhao, M.H., Lai, C., Wei, Z., Huang, C., Xie, G.X., Liu, Z.F. 2012b. Use of iron oxide nanomaterials in wastewater treatment: A review. *Science of the Total Environment*, **424**, 1-10.

Yang, L., Zheng, X., Liu, M., Luo, S., Luo, Y., Li, G. 2017a. Fast photoelectro-reduction of CrVI over MoS2@TiO2 nanotubes on Ti wire. *Journal of Hazardous Materials*, **329**, 230-240.

Yang, Q., Wang, Y., Wang, J., Liu, F., Hu, N., Pei, H., Yang, W., Li, Z., Suo, Y., Wang, J. 2018a. High effective adsorption/removal of illegal food dyes from contaminated aqueous solution by Zr-MOFs (UiO-67). *Food Chem*, **254**, 241-248.

Yang, Q.F., Wang, J., Chen, X.Y., Yang, W.X., Pei, H.N., Hu, N., Li, Z.H., Suo, Y.R., Li, T., Wang, J.L. 2018b. The simultaneous detection and removal of organophosphorus pesticides by a novel Zr-MOF based smart adsorbent. *Journal of Materials Chemistry A*, **6**(5), 2184-2192.

Yang, Q.F., Wang, J., Zhang, W.T., Liu, F.B., Yue, X.Y., Liu, Y.N., Yang, M., Li, Z.H., Wang, J.L. 2017b. Interface engineering of metal organic framework on graphene oxide with enhanced adsorption capacity for organophosphorus pesticide. *Chemical Engineering Journal*, **313**, 19-26.

Ye, S., Zeng, G., Wu, H., Zhang, C., Dai, J., Liang, J., Yu, J., Ren, X., Yi, H., Cheng, M., Zhang, C. 2017a. Biological technologies for the remediation of co-contaminated soil. *Critical Reviews in Biotechnology*, **37**(8), 1062-1076.

Ye, S.J., Zeng, G.M., Wu, H.P., Zhang, C., Liang, J., Dai, J., Liu, Z.F., Xiong, W.P., Wan, J., Xu, P.A., Cheng, M. 2017b. Co-occurrence and interactions of pollutants, and their impacts on soil remediation-A review. *Critical Reviews in Environmental Science and Technology*, **47**(16), 1528-1553.

Zeng, G., Wu, H., Liang, J., Guo, S., Hu, L., Xu, P., Liu, Y., Yuan, Y., He, X., He, Y. 2015. Efficiency of biochar and compost (or composting) combined amendments for reducing Cd, Cu, Zn and Pb bioavailability, mobility and ecological risk in wetland soil. *Rsc Advances*, **5**(44), 34541-34548.

Zhang, C., Lai, C., Zeng, G., Huang, D., Yang, C., Wang, Y., Zhou, Y., Cheng, M. 2016. Efficacy of carbonaceous nanocomposites for sorbing ionizable antibiotic sulfamethazine from aqueous solution. *Water Research*, **95**, 103-12.

Zhang, M., Gao, B., Yao, Y., Xue, Y., Inyang, M. 2012. Synthesis, characterization, and environmental implications of graphene-coated biochar. *Science of the Total Environment*, **435-436**, 567-72.

Zhang, Y., Zeng, G.M., Tang, L., Chen, J., Zhu, Y., He, X.X., He, Y. 2015. Electrochemical sensor based on electrodeposited graphene-Au modified electrode and nanoAu carrier amplified signal strategy for attomolar mercury detection. *Anal Chem*, **87**(2), 989-96.

Zhao, G.X., Li, J.X., Wang, X.K. 2011. Kinetic and thermodynamic study of 1-naphthol adsorption from aqueous solution to sulfonated graphene nanosheets. *Chemical Engineering Journal*, **173**(1), 185-190.

Zhao, Y., Zhang, X., Wang, C., Zhao, Y., Zhou, H., Li, J., Jin, H. 2017. The synthesis of hierarchical nanostructured MoS 2 /Graphene composites with enhanced visible-light photo-degradation property. *Applied Surface Science*, **412**, 207-213.

Zhou, C.Y., Lai, C., Huang, D.L., Zeng, G.M., Zhang, C., Cheng, M., Hu, L., Wan, J., Xiong, W.P., Wen, M., Wen, X.F., Qin, L. 2018. Highly porous carbon nitride by supramolecular preassembly of monomers for photocatalytic removal of sulfamethazine under visible light driven. *Applied Catalysis B-Environmental*, **220**, 202-210.

Zhou, W.J., Hou, D.M., Sang, Y.H., Yao, S.H., Zhou, J., Li, G.Q., Li, L.G., Liu, H., Chen, S.W. 2014. MoO2 nanobelts@nitrogen self-doped MoS2 nanosheets as effective electrocatalysts for hydrogen evolution reaction. *Journal of Materials Chemistry A*, **2**(29), 11358-11364.

Zhu, C., Zhang, L., Jiang, B., Zheng, J., Hu, P., Li, S., Wu, M., Wu, W. 2016. Fabrication of Z-scheme Ag 3 PO 4 /MoS 2 composites with enhanced photocatalytic activity and stability for organic pollutant degradation. *Applied Surface Science*, **377**, 99-108.

**Figure captions**

**Fig. 1** Schematic illustration of the formation of *g*-$MoS_2$-BC composite and its application for removal of TC

**Fig. 2** SEM images of pristine biochar (a), pure $MoS_2$ (b), *g*-$MoS_2$-BC (c), and $MoS_2$ sheets on *g*-$MoS_2$-BC composite (d), and HRTEM images of *g*-$MoS_2$-BC (e and f)

**Fig. 3** (a) The pore-size distribution curve of *g*-$MoS_2$-BC and TC-loaded *g*-$MoS_2$-BC, inset shows $N_2$ adsorption-desorption isotherms of *g*-$MoS_2$-BC at 77 K; (b) XRD patterns of pure $MoS_2$, *g*-$MoS_2$-BC and TC-loaded *g*-$MoS_2$-BC; (c) FT-IR spectrums of pure $MoS_2$, *g*-$MoS_2$-BC and TC-loaded *g*-$MoS_2$-BC, (d) XPS survey spectra of pristine biochar and *g*-$MoS_2$-BC

**Fig. 4** The XPS spectra of *g*-$MoS_2$-BC composite: high resolution XPS spectrum of Mo 3d and S 2s (a), S 2p (b), C 1s (c), and O 1s (d)

**Fig. 5** (a) Zeta potentials of *g*-$MoS_2$-BC at different pH ranging from 2.0-11.0 and the effect of pH values, (b) effect of ionic strength on adsorption capacity of *g*-$MoS_2$-BC for TC. Error bars represent standard error of the mean (n=3). Different letters indicate significant difference ($p<0.05$) between each salt concentration.

**Fig. 6** Effect of contact time on the adsorption of TC onto *g*-$MoS_2$-BC (a); the pseudo-first-order plots (b), pseudo-second-order plots (c), intra-particle diffusion plots (d), Boyd plots (e) and Bangham plots (f) for TC adsorption by *g*-$MoS_2$-BC

**Fig. 7** The proposed mechanisms for the removal behavior of TC onto *g*-$MoS_2$-BC

**Table 1 Adsorption kinetics parameters of pseudo-first-order kinetic, pseudo-second-order kinetic and Bangham model for TC on *g*-$MoS_2$-BC**

| Concentration (mg/L) | Pseudo-first-order kinetic | | | | Pseudo-second-order kinetic | | | Bangham model | | |
|---|---|---|---|---|---|---|---|---|---|---|
| | $q_{e,exp}$ (mg/g) | $k_1$ (1/h) | $q_{e,cal}$ (mg/g) | $R^2$ | $k_2$ (g/mg.h) | $q_{e,cal}$ (mg/g) | $R^2$ | $k_B$ | m | $R^2$ |
| **50** | 103.676 | 0.002303 | 31.225 | 0.9428 | 0.000465 | 104.167 | 0.9994 | 49.957 | 9.560 | 0.9672 |
| **100** | 174.285 | 0.002763 | 58.144 | 0.9448 | 0.000248 | 175.438 | 0.9993 | 83.714 | 9.701 | 0.9876 |
| **150** | 208.583 | 0.002994 | 66.911 | 0.9807 | 0.000203 | 209.643 | 0.9992 | 113.083 | 11.936 | 0.9927 |

**Table 2 The obtained parameters' value of intra-particle and Boyd's film-diffusion models**

| Kinetics models | Parameters | | Initial concentration (mg/L) | | |
|---|---|---|---|---|---|
| | | | 50 | 100 | 150 |
| **Intra-particle diffusion** | $K_{id}$ $(mg/g{\bullet}min^{1/2})$ | $K_{1d}$ | 4.986 | 5.403 | 4.738 |
| | | $K_{2d}$ | 1.225 | 2.316 | 2.058 |
| | | $K_{3d}$ | 0.244 | 0.516 | 0.484 |
| | $C_i$ | $C_1$ | 45.502 | 87.822 | 122.691 |
| | | $C_2$ | 69.932 | 111.834 | 146.113 |
| | | $C_3$ | 93.766 | 153.521 | 188.554 |
| | $R_i^2$ | $R_1^2$ | 0.9694 | 0.9580 | 0.9831 |
| | | $R_2^2$ | 0.9524 | 0.9691 | 0.9854 |
| | | $R_3^2$ | 0.8063 | 0.8691 | 0.9425 |
| **Boyd's film-diffusion** | $R_i^2$ | $R_1^2$ | 0.9468 | 0.9724 | 0.9702 |
| | | $R_2^2$ | 0.9947 | 0.9673 | 0.9771 |

**Table 3 The obtained results of isotherm models for TC adsorption**

| Isotherm models | Parameters | Temperature (K) | | |
|---|---|---|---|---|
| | | 298 | *308* | *318* |
| **Langmuir** | $R^2$ | 0.9927 | 0.9919 | 0.9913 |
| | $K_L$ *(L/mg)* | 0.0553 | 0.0637 | 0.0887 |
| | $q_{max}$ *(mg/g)* | 249.376 | 423.728 | 699.301 |
| | $R_L$ | 0.0692 | 0.0803 | 0.1017 |
| **BET model** | $R^2$ | 0.9981 | 0.9953 | 0.9928 |
| | $K_b$ | 4430.910 | 3202.787 | 2782.223 |
| | $q_{max}$ *(mg/g)* | 248.561 | 422.385 | 696.492 |
| **Freundlich** | $R^2$ | 0.9473 | 0.9745 | 0.9772 |
| | $K_F$ *(L/mg)* | 30.372 | 40.988 | 64.508 |
| | *1/n* | 0.447 | 0.497 | 0.529 |
| **Temkin** | $R^2$ | 0.9651 | 0.9358 | 0.9169 |
| | $K_T$ *(L/mg)* | 73.402 | 136.687 | 142.263 |
| | $B_T$ | 30.154 | 40.119 | 51.088 |
| | $b_T$ *(J/mol)* | 82.246 | 63.889 | 57.799 |
| **D-R model** | $R^2$ | 0.8138 | 0.7713 | 0.7604 |
| | *E (kJ/mol)* | 0.863 | 0.992 | 1.107 |
| | $q_{max}$ *(mg/g)* | 168.891 | 243.464 | 315.977 |

**Fig. 1**

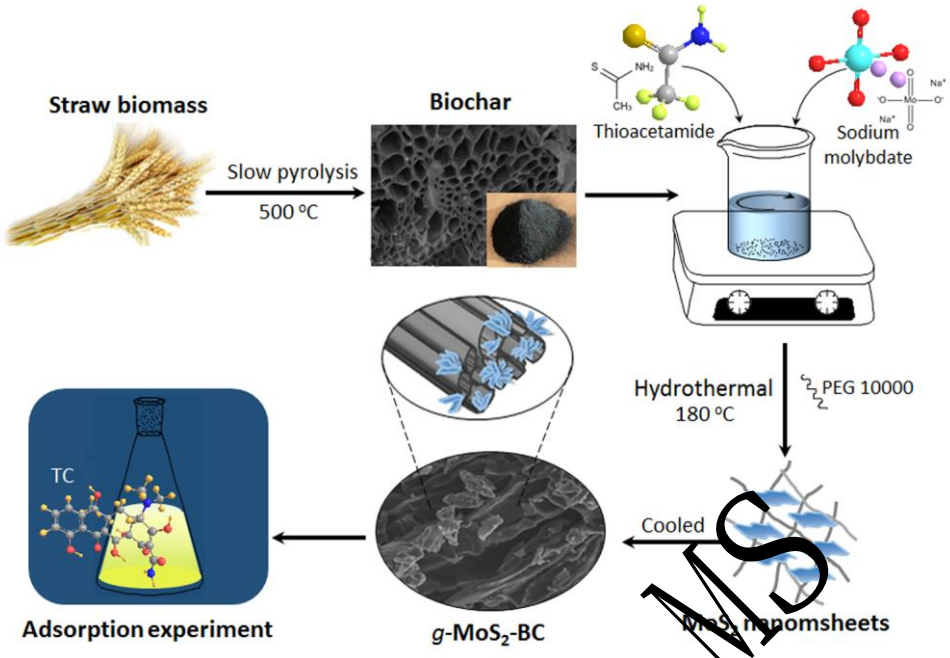

**Fig. 2**

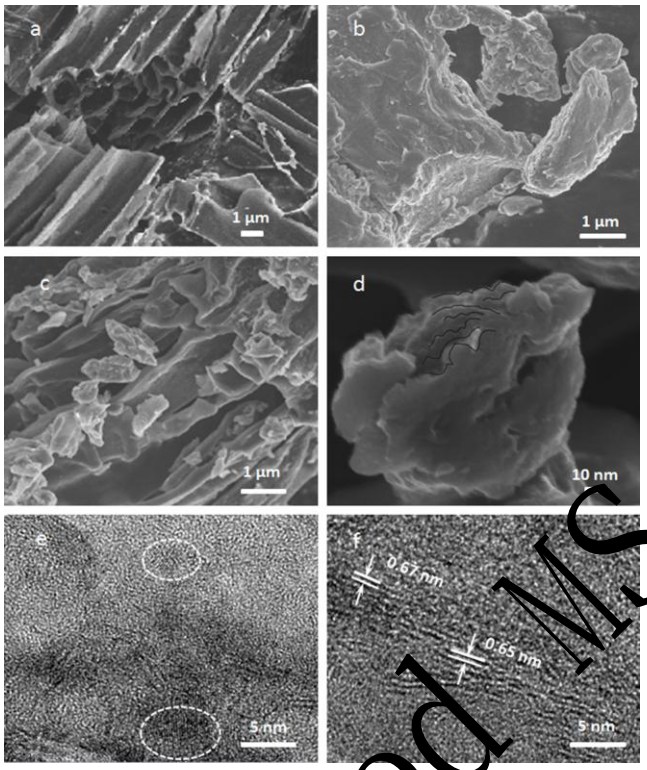

**Fig. 3**

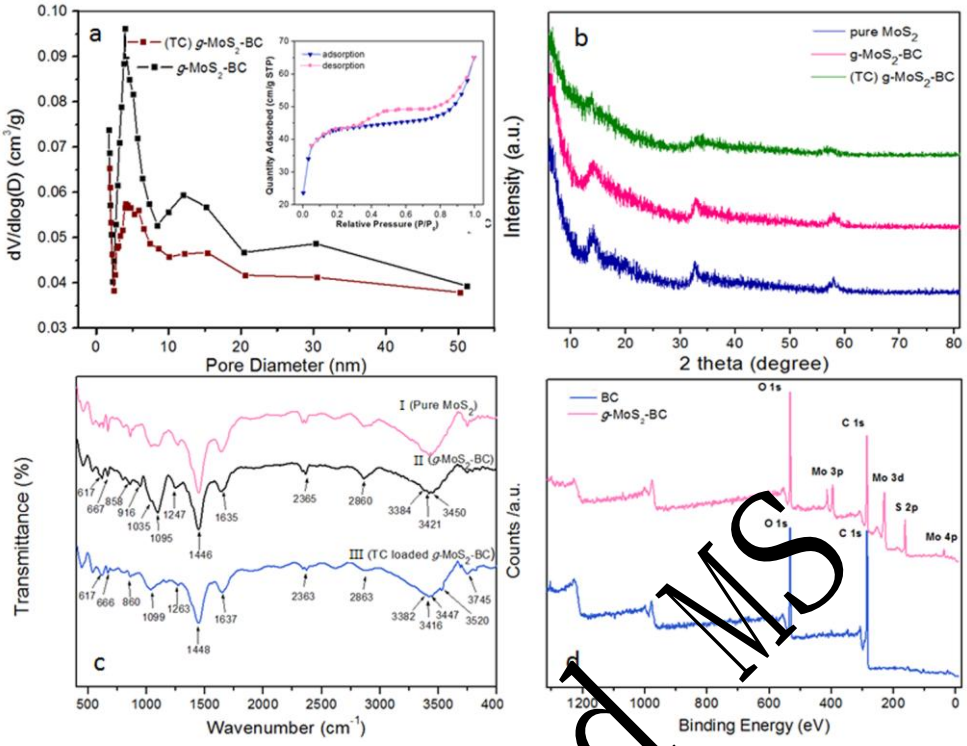

**Fig. 4**

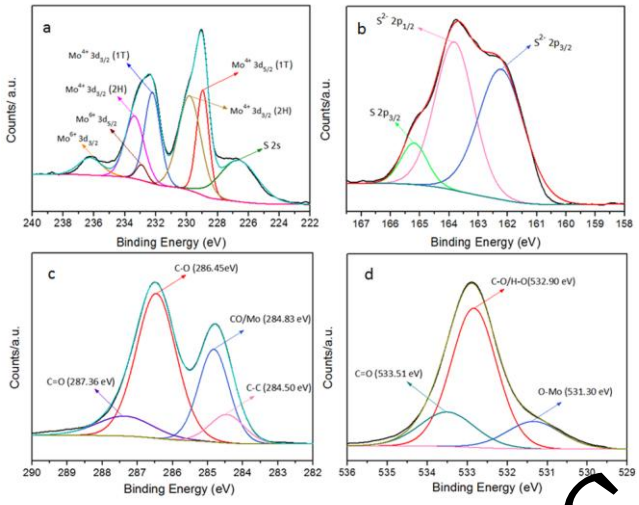

**Fig. 5**

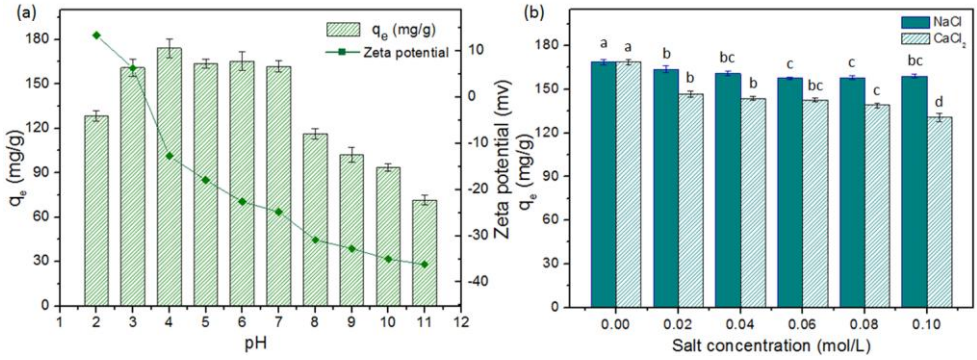

**Fig. 6**

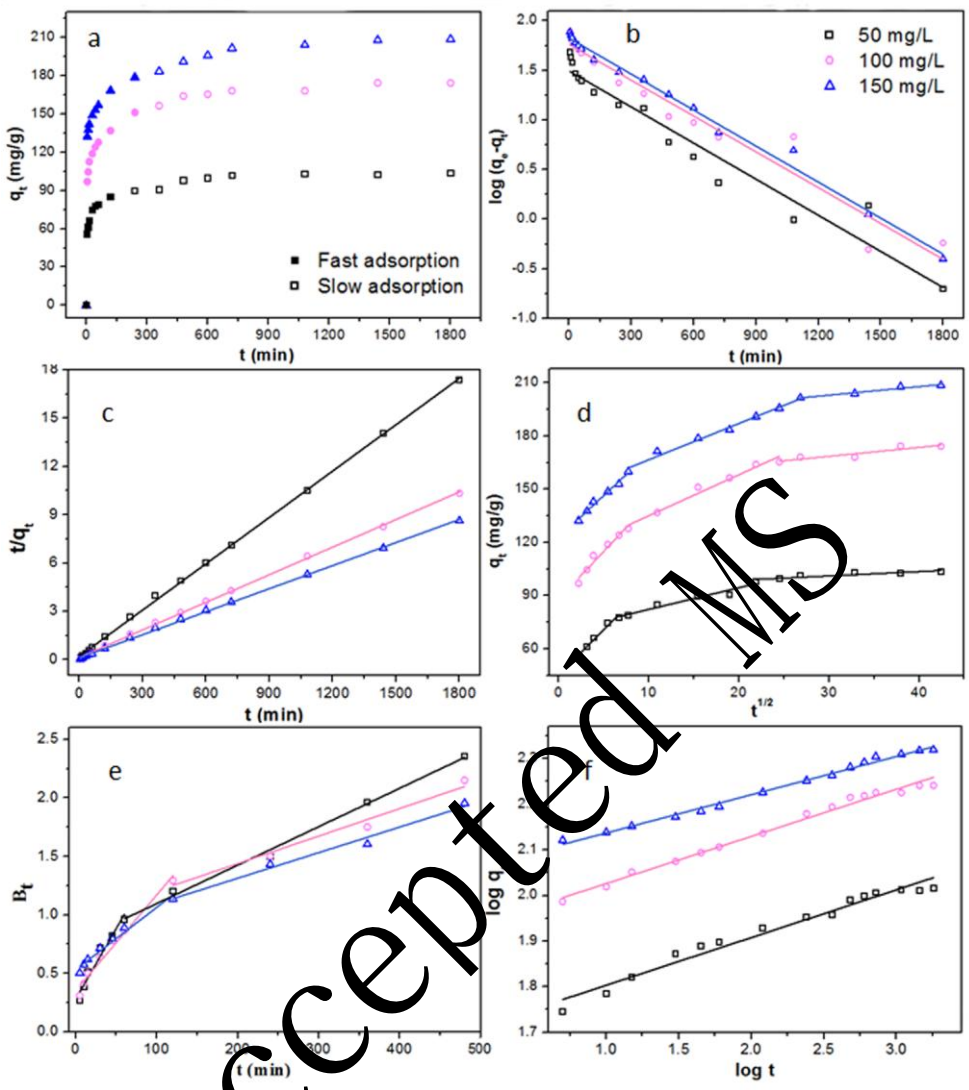

**Fig. 7**